

AAV variant enables human T cell engineering *in vivo*

2 Zhike Lu^{1,2,3*}, Ke Ni^{1,2,3*}, Wenjun Liu^{4*}, Qingkai Song^{1,2}, Rong Zheng^{1,2}, Ming Wei³, Yinling
3 Zhang², Jing Wang^{1,2}, Lina Wei³, Chenlu Wu^{2,3}, Qingfeng Zhang³, Jiamei Wu³, Rujie Zhu⁵, Shuai
4 Ding⁵, Chunyu Cheng⁴, Yanyi Cong³, Yinxia Xu³, Baorui Kong³, Shanshan Wu³, Gang Wang³,
5 Xiaojuan Wang², Yalin Wang², Xu Qian⁶, Ruixia Deng³, Hui Chen³, Yan Li^{4,7,8#}, Lijia Ma^{1,2,3#}

6 ¹Westlake Laboratory, Hangzhou, Zhejiang, 310024, China

7 ²School of Life Sciences, CryoEM Core Facility, Westlake University, Hangzhou, Zhejiang,
8 310030, China

9 ³Westlake Genetech, Hangzhou, Zhejiang, 310024, China

10 ⁴MOE Key Laboratory of Model Animal for Disease Study, Model Animal Research Center,
11 Department of Oncology, Nanjing Drum Tower Hospital, The Affiliated Hospital of Medical
12 School, Nanjing University, Nanjing, Jiangsu, 210061, China.

13 ⁵Department of Rheumatology and Immunology, Nanjing Drum Tower Hospital, The Affiliated
14 Hospital of Medical School, Nanjing University, Nanjing, 211166, China

15 ⁶Department of Clinical Laboratory, Zhejiang Cancer Hospital, Hangzhou Institute of Medicine,
16 Chinese Academy of Sciences, Hangzhou, Zhejiang, 310022, China

17 ⁷ChemBioMed Interdisciplinary Research Center at Nanjing University, Nanjing 210061, China.

18 ⁸Wuxi Xishan NJU Institute of Applied Biotechnology, Wuxi, Jiangsu, 214101, China.

19

20 *These authors contributed equally to this work.

21 #Corresponding author: Lijia Ma, malijia@westlake.edu.cn; Yan Li, yanli@nju.edu.cn

22

23 **Abstract**

24 Autologous chimeric antigen receptor T (CAR-T) cell therapy has demonstrated
25 therapeutic effectiveness in hematologic malignancies and autoimmune diseases.
26 However, the manufacturing complexity and the required lymphodepletion hindered its
27 wide clinical application. Engineering human T cells *in vivo* holds promise to conquer
28 these limitations but requires effective T cell-targeted CAR delivery with demonstrated

29 safety. Here, we show that an engineered AAV6 variant, AAV6-M2, can enable *in vivo*
30 CAR expression in human T cells following systemic administration in a Humanized
31 Immune System (HIS) mouse model. AAV6-M2-CD19CAR turned up to 85.2% of human
32 CD8⁺ T cells into CAR-T cells across multiple organs six weeks post-AAV injection. In HIS
33 mice exhibiting systemic lupus erythematosus (SLE)-like symptoms, AAV6-M2-
34 CD19CAR treatment effectively depleted B cells in both peripheral blood and tissues,
35 accompanied by improved lupus pathologies. Importantly, systemic delivery of AAV6-M2
36 resulted in significant liver de-targeting, with viral genome levels in the liver reduced by
37 over two orders of magnitude in both mice and cynomolgus macaque compared to the
38 wild-type AAV. Through CRISPR screening, cryo-EM structural analysis, and molecular
39 docking, we identified CD62L as a key mediator of AAV6-M2's enhanced transduction to
40 human T cells, enabling CAR delivery without the need for prior T cell activation. These
41 findings established that AAV-mediated CAR delivery can generate functional human
42 CAR-T cells *in vivo*, with mechanistic insights into the selective targeting of T cells. This
43 work highlights engineered AAV vectors as a promising platform for *in vivo* CAR-T therapy
44 and expands the therapeutic landscape of AAV beyond inherited diseases.

45

46 **Introduction**

47 *Ex vivo* CAR-T cell therapy has shown remarkable success in treating both malignant and
48 autoactivated B cells¹. This therapy has led to high rates of long-lasting remission in
49 patients with relapsed or refractory cancers or autoimmune diseases who previously had
50 limited treatment options. Despite its success, challenges remain for the current FDA-
51 approved autologous CAR-T therapy, which is personalized and requires the collection of
52 a patient's T cells, genetic modifications to express CARs, and lymphodepletion prior to
53 CAR-T cell infusion². Off-the-shelf CAR-T therapy, also called allogeneic CAR-T, uses T
54 cells from donors or derived from iPSC, providing immediate availability of the CAR-T cell
55 product¹. However, issues of allogeneic CAR-T include life-threatening graft-versus-host
56 diseases (GvHD) and rapid elimination by the host immune system³.

57 *In vivo* CAR-T cell therapy involves delivering the CAR sequence directly into the patient's
58 T cells within their body. CAR sequence is packed by viral or non-viral delivery platforms,

59 which is also “off-the-shelf” while bypassing the GvHD of allogeneic CAR-T cell therapy.
60 In this context, *in vivo* CAR-T is no longer a personalized cell therapy but a ready-to-use
61 gene therapy. Thus, it faces the same challenge as gene therapy: efficiently and
62 specifically delivering the CAR sequence to T cells. Several delivery platforms have been
63 used to develop *in vivo* CAR-T therapy. Lipid nanoparticles (LNP) packing mRNA-
64 encoding CAR sequence have been conjugated with antibodies, including anti-CD3, CD8,
65 and CD5, to achieve redirection to T cells rather than the liver *in vivo*⁴⁻⁹. Although the
66 COVID-19 vaccine has proved the safety and scalability of this platform, antibody-
67 conjugated LNPs face challenges in large-scale manufacturing and unclear long-term
68 clinical safety following intravenous administration. Lentivirus (LV) with an engineered
69 envelope with single-chain variable fragments (scFv) against-CD3, CD4, CD7, CD8, or
70 TCR could also be redirected to T cells *in vivo*¹⁰⁻¹⁶. LV integrates the CAR sequence into
71 the host cell genome, allowing stable transgene expression through T-cell expansion
72 while also raising safety concerns on sequence integration into the genome of bystander
73 cells and insertional mutagenesis. Virus-like particles (VLPs) resemble viruses but lack
74 viral genetic material, making them non-infectious^{17,18}. VLP allows *in vivo* delivery of
75 Ribonucleoprotein (RNP) instead of DNA. A recent study engineered VLP by pairing the
76 display of a mutated VSVG anti-CD3, CD4, or CD28 scFv on Cas9-EDVs (enveloped
77 delivery vehicles) to target T cells *in vivo* and deliver genome editor and CAR sequences¹⁹.
78 Although a proven concept, the less efficient generation of CAR-T cells *in vivo* and the
79 complicated manufacturing process hinder its applications in clinics.
80 Recombinant AAV vectors (AAVs) have been widely used in gene therapy due to their
81 safety profile and ability to induce long-term expression of transgenes in non-dividing cells.
82 Although wild-type AAVs naturally accumulate in the liver by systemic injection,
83 engineering the variable regions of the capsid protein of AAV has proved to be effective
84 in redirecting AAV to extrahepatic organs or tissues (e.g., the central nervous system and
85 muscles) or increasing transduction efficiencies to non-hepatic cells²⁰. For example,
86 DART-AAV inserted a designed ankyrin repeat protein (DARPin) targeting murine CD8
87 into the GH2-GH3 loop of AAV2 capsid protein VP1 and resulted in over 20-fold increase
88 of transduction activity in murine T cells than AAV2¹⁰. Ark313 is an AAV6 variant targeting
89 murine T cells, which was engineered from three rounds of directed evolution of a capsid

90 library with 7-mer random insertion in the variable region IV²¹. Infusion of Ark313-
91 generated CAR-T cells demonstrated better efficacy in controlling tumor growth than
92 retrovirus-generated CAR-T cells. In a follow-up study, intravenous Ark313 injection
93 successfully transduced murine T cells *in vivo*²². However, the question of whether an
94 engineered AAV variant could enable the *in vivo* targeting of human T cells, while staying
95 away from the liver and other organs, through systemic delivery has yet to be explored.

96 Here, we demonstrated that an engineered AAV6 variant, AAV6-M2, can effectively
97 engineer human T cells both *in vitro* and *in vivo*. *In vitro*, AAV6-M2 successfully delivers
98 the CD19 CAR sequence into both activated and resting human T cells, leading to robust,
99 antigen-dependent cytotoxicity. Further, evidence from whole-genome CRISPR
100 screening, targeted gene knockout, cryo-EM structural analysis, and molecular docking
101 collectively underscores the critical role of CD62L, a cell surface marker of less-
102 differentiated T cells²³, in facilitating AAV6-M2 transduction into resting T cells without
103 prior activation. Systemic administration of AAV6-M2-CAR into human immune system
104 (HIS) mice resulted in the generation of up to 85.2% of CAR-T cells six weeks post AAV
105 injection. In the HIS mice with systemic lupus erythematosus (SLE), this approach
106 successfully ameliorated lupus pathologies, correlating with the depletion of both
107 circulating and tissue-resident B cells. Notably, systemic injection of AAV6-M2 led to
108 approximately two orders of magnitude lower liver accumulation compared to wild-type
109 AAV, in both mouse and cynomolgus macaque, highlighting a favorable safety profile.
110 Collectively, this study positions AAV6-M2 as a clinically translatable vector for *in vivo*
111 CAR-T therapy and broadens the therapeutic scope of AAV-based gene delivery from
112 inherited disorders to autoimmune diseases.

113

114 **Results**

115 **AAV6 variants show superior transduction efficiencies in human primary T cells**

116 To design a capsid library with an improved likelihood of identifying variants with specific
117 tropism for human T cells, we collected functional peptides reported from publicly
118 available databases and literature. For these peptide sequences, we randomly selected

119 fragments with 6-12 amino acids and inserted them between residues A581 and T593 of
120 the AAV6 capsid protein VP3 (variable region VIII or VR VIII)²⁴, yielding a diverse library
121 comprising approximately 480,000 AAV6 variants. Following capsid library screening in
122 human primary T cells, we identified variants that exhibited enhanced transduction
123 efficiencies relative to wild-type AAV6 (AAV6-WT). Among them, two top-performing
124 candidates, designated AAV6-M1 and AAV6-M2, were selected based on their
125 transduction efficiencies and low coefficient of variation in transduction performance
126 across replicates (**Supplementary Figure 1A**).

127 To validate the transduction efficiencies of the leading candidates in human primary T
128 cells, we packaged self-complementary AAVs encoding EGFP using the AAV6-M1 and
129 AAV6-M2 capsids and compared their performance to AAV6-WT (**Figure 1A**).
130 Transduction efficiency was quantified by measuring the percentage of EGFP⁺ T cells.
131 Across a range of multiplicities of infection (MOI; 1×10^2 , 1×10^3 , and 1×10^4), both
132 AAV6-M variants outperformed AAV6-WT (**Figure 1B**). This superiority was consistent
133 when assessing both the percentage of EGFP⁺ cells and the mean fluorescent intensity
134 (MFI) (**Figure 1C-D**). Notably, at an MOI of 1×10^3 , the AAV6-M1 and AAV6-M2 achieved
135 EGFP⁺ rates of 91.8% and 80.2%, respectively – matching or exceeding the transduction
136 efficiency observed with AAV6-WT at an MOI one order of magnitude higher (1×10^4).
137 Moreover, the engineered AAV6-M2 exhibited packaging efficiency comparable to that of
138 AAV6-WT, whereas AAV6-M1 showed a reduced packaging yield (**Supplementary**
139 **Figure 1B**). The manufacturability of AAV6-M2 was further verified in a scaled-up 3-liter
140 bioreactor, demonstrating comparable packaging efficiency to AAV6-WT, a dominant full-
141 particle peak, and uniform capsid morphology (**Supplementary Figure 1C-E**).

142

143 **CD62L mediates enhanced transduction of AAV6-M2 in human T cells**

144 AAV6-M variants were assembled using engineered capsid proteins containing mutations
145 between residues A581 and T593 of VP3, where the corresponding peptides are located
146 in the 3-fold protrusion of AAV particles and are positioned to interact directly with host
147 cells. We hypothesized that these variants utilized distinct cell-surface factors to enter
148 human T cells, compared to AAV6-WT. To investigate this, we performed a whole-genome

149 CRISPR knockout screen in Jurkat cells to identify genes contributing to the enhanced
150 transduction efficiencies of AAV6-M variants (**Figure 2A**). In brief, Jurkat cells stably
151 expressing SpCas9 (Jurkat-Cas9) were first transduced with the lentiviral CRISPR
152 Brunello library at a low MOI to deliver one sgRNA per cell, followed by transduction with
153 either AAV6-WT-EGFP, AAV6-M1-EGFP, or AAV6-M2-EGFP. We then sorted and
154 collected the top and bottom 20% EGFP⁺ Jurkat-Cas9 cells. Compared to the top 20%,
155 sgRNAs enriched in the bottom 20% of cells represented gene knockouts that disrupted
156 the AAV attachment, internalization, or intracellular trafficking in human T cells.

157 We analyzed the top 10 genes enriched in each of the three CRISPR screens. All screens
158 identified genes that are known to be essential for AAV transduction and trafficking,
159 including KIAA0319L (AAVR) and TM9SF2, validating the effectiveness of our screening
160 approach. A few genes, such as *NOTCH1*, were specifically enriched in the screen using
161 AAV6-M1 relative to AAV6-WT (**Supplementary Figure 2A**). However, *NOTCH1* is
162 broadly expressed across multiple organs, including endocrine tissues, brain, and liver,
163 which is less favorable for in vivo T cell targeting. Nevertheless, among the top 10 genes
164 specifically enriched in the AAV6-M2 screen, *SELL* stood out (**Figure 2B-C**). *SELL*
165 encodes a cell surface protein and is almost exclusively expressed in immune cells. Also
166 known as CD62L or L-selectin, *SELL* is essential for the binding and rolling of lymphocytes
167 on endothelial cells, facilitating their migration into secondary lymphoid organs.
168 Interestingly, a recent study engineered lentiviral envelopes with CD62L-specific scFv to
169 enable CAR delivery into less differentiated human T cells²⁵.

170 Indeed, knocking out CD62L (*SELL*) from Jurkat cells significantly reduced the
171 transduction efficiency of AAV6-M2 but not AAV6-WT (**Figure 2D**). The reduction was
172 comparable to that observed upon AAVR knockout, suggesting a critical and specific role
173 of CD62L in mediating AAV6-M2 entry into T cells. Moreover, we used two independent
174 sgRNAs to knock out CD62L in primary human T cells from three donors. Following
175 CD62L knockout, the transduction efficiency of AAV6-M2 was markedly diminished, while
176 AAV6-WT transduction remained largely unaffected (**Figure 2E, Supplementary Figure**
177 **2B**). Collectively, both CRISPR screening and targeted gene knockout experiments

178 underscore the essential role of CD62L in AAV6-M2 transduction into human T cells – a
179 mechanism that appears unique to this AAV variant and is not shared by wild-type AAV6.
180 To further investigate how the engineered loop may enhance the interaction between
181 AAV6-M2 and CD62L, we resolved the cryo-EM structure of AAV6-M2 at 1.8 Å resolution
182 (**Figure 2F, Supplementary Figure 2C**). The VP protein monomer was accurately
183 modeled, with both the backbone and side chains in the VR VIII loop clearly resolved
184 (**Supplementary Figure 2D**). Structural alignment showed that the backbone
185 conformation of AAV6-M2 is nearly identical to that of wild-type AAV6 (PDB: 4V86)
186 (**Supplementary Figure 2E**); however, the side chain conformations within the VR VIII
187 loop differ substantially (**Supplementary Figure 2F-G**). To explore potential interactions
188 with CD62L, we performed molecular docking between AAV6-M2 and human CD62L
189 (PDB: 5VC1; lectin/EGF domains). The engineered loop was predicted to insert into the
190 EGF domain of CD62L, where three negatively charged residues (E590, E591, and E592)
191 within the VR VIII loop of AAV6-M2 engage a positively charged surface pocket through
192 electrostatic interactions (**Figure 2G-H**). These structural observations suggest that the
193 engineered VR VIII loop appears to contribute to enhancing the engagement between
194 AAV6-M2 and CD62L. The engineered loop, however, did not increase but slightly
195 reduced neutralization by human serum compared to AAV6-WT (**Figure 2I**,
196 **Supplementary Figure 2J**).

197

198 **AAV6-M2 transduces resting human T cells *in vitro***

199 Considering both the efficiencies of viral packaging and the specificity of the binding
200 partner, we focused on AAV6-M2 in the subsequent studies. We first replaced the
201 transgene with CD19 CAR to evaluate the expression kinetics and cytotoxicity of AAV6-
202 M2-mediated CAR-T cells *in vitro* (**Supplementary Figure 3A**). Following transduction of
203 bead-activated human T cells (aT) with AAV6-M2-CAR, the proportion of CAR⁺ T cells
204 peaked at day 3 and gradually declined by day 10 (**Figure 3A**). We observed comparable
205 T cell viability and proliferation relative to the non-AAV control (**Figure 3B**,
206 **Supplementary Figure 3B**). When co-cultured with CD19-expressing NALM6 cells,
207 AAV6-M2-transduced T cells exhibited robust cytotoxicity by 20 hours post-transduction

208 and achieved complete B cell killing by day 3 (**Figure 3C-D, Supplementary Figure 3C**).
209 In contrast, AAV6-WT-transduced T cells show minimal cytotoxicity. These results
210 demonstrate that AAV6-M2 effectively delivers CD19 CAR to active human T cells,
211 enabling antigen-specific cytotoxicity *in vitro*.

212 Next, we performed site-specific CD19 CAR insertion using two AAV6-M2 vectors to
213 generate stable CAR-expressing T cells, a strategy expected to prolong CAR-T presence
214 during T-cell proliferation. The AAV vector-1 provides the CD19 CAR expression cassette,
215 which is integrated into the 1st exon of *TRAC*, where the AAV vector-2 generates a
216 double-strand break by enAsCas12f-mediated cleavage (**Figure 3E**). Following dual AAV
217 transduction, transient CAR⁺ T cells (TCR⁺CAR⁺) emerged rapidly but declined after day
218 3 (**Figure 3F**), coinciding with the onset of robust T-cell expansion (**Figure 3G**). In contrast,
219 stable CAR⁺ T cells (TCR⁻CAR⁺) gradually increased over time, expanding in parallel with
220 the proliferating T cell population and exhibiting sustained CAR expression. Together,
221 these results demonstrate that AAV6-M2 enables efficient generation of stable CAR⁺ T
222 cells through precise genomic integration of the CAR cassette, thereby supporting
223 prolonged CAR-T expression during T-cell proliferation.

224 However, since the majority of human T cells are in a resting state *in vivo*, we sought to
225 evaluate the delivery capability of AAV6-M2 in non-activated T cells. In two parallel
226 experiments, non-activated human T cells were transduced with AAV6-M2-EGFP and
227 subsequently either activated or left unstimulated (**Supplementary Figure 3D-E**). We
228 then monitored the EGFP expression over time. Interestingly, in the absence of activation,
229 the percentage of EGFP⁺ cells gradually increased, reaching approximately 40% by day
230 15 (**Figure 3H**). In contrast, post-transduction activation rapidly elevated the percentage
231 of EGFP⁺ cells to ~80% within three days, followed by a decline to levels similar to those
232 observed in non-activated cells by the endpoint of the experiment (**Figure 3I**). These
233 results indicate that AAV6-M2 is capable of delivering a transgene into human T cells
234 without the need for prior or subsequent activation.

235 To investigate the antigen-specific cytotoxic potential of core circulating T cell subsets
236 following AAV6-M2-CAR transduction, we co-cultured naïve (Tn), central memory (TCM),
237 and effector memory (TEM) T cells with NALM6 cells (**Figure 3J**). In the absence of bead-

238 based activation, Tn cells effectively eliminated NALM6 cells between days 6 and 9 post-
239 co-culture, with some variability observed among donors (**Figure 3K**). The cytotoxic
240 activities of TCM and TEM were more variable, with two donors exhibiting complete
241 NALM6 clearance between days 6 and 14 (**Supplementary Figure 3F-G**). Upon antigen
242 stimulation, both Tn and TCM underwent phenotypic conversion into TEM
243 (**Supplementary Figure 3H-J**). Collectively, AAV6-M2 enables effective CAR delivery to
244 multiple resting T cell subsets and supports their differentiation into functional effectors
245 capable of eliminating target cells in an antigen-dependent manner.

246

247 **AAV6-M2 mediates *in vivo* CAR-T cell generation and B cell depletion**

248 The AAV-mediated CAR-T cell generation encouraged us to explore the *in vivo* application
249 of AAV6-M2. We are curious whether the superior transduction efficiency of AAV6-M2 to
250 human T cells could enable the generation of CAR-T cells *in vivo* through systemic
251 administration to bypass the *ex vivo* manufacturing process of the conventional CAR-T
252 cell therapy. We employed an optimized Human Immune System (HIS) mouse model
253 (NCG-X-hIL15), in which human hematopoietic stem cells (hHSCs) were engrafted into
254 immunodeficient mice and various human immune subsets were developed (**Figure 4A**).
255 Following engraftment, HIS mice with comparable levels of human T and B cells were
256 randomly grouped (**Supplementary Figure 4A-B**) and systemically injected with AAV6-
257 WT (n = 6) or AAV6-M2 (n = 8) at a dose of 3×10^{13} vg/kg and sacrificed after 28 or 42
258 days. The same CD19 CAR-EGFP construct used in the *in vitro* assay was applied in the
259 *in vivo* experiment.

260 In peripheral blood, CAR⁺ T cells emerged by week 2 following AAV6-M2-CAR injection,
261 whereas very few CAR⁺ T cells were detected in the AAV6-WT-CAR group (**Figure 4B**).
262 These CAR⁺ cells were predominantly CD8⁺, with minimal CD4⁺ CAR⁺ T cells detected
263 (**Figure 4C**). Concurrently, human B cells, the targeted cells of these CAR⁺ T cells,
264 decreased over time. The AAV6-M2-CAR group showed a notable decline from baseline
265 to week 4, with B cell counts in most mice approaching the detection threshold
266 (**Supplementary Figure 4C-D**). While B cell levels were variable at baseline and across

267 individual mice, the overall trend indicated a greater extent of reduction in the AAV6-M2-
268 CAR group by the study endpoint, compared to the AAV6-WT-CAR group.

269 In bone marrow, spleen, liver, and lung, the human B cells were largely undetectable in
270 AAV6-M2-treated mice, whereas significantly more B cells remained in mice treated with
271 AAV6-WT (**Figure 4D**). Correspondingly, CAR⁺ T cells were readily detected in these
272 organs in the AAV6-M2-CAR group, but were largely absent in the AAV6-WT-CAR group
273 (**Figure 4E**). Mirroring the observation from the peripheral blood, CAR⁺ T cells were
274 predominantly CD8⁺, with up to 85.2% CAR⁺ CD8⁺ present in the bone marrow at week
275 6 (**Figure 4F, Supplementary Figure 4E**). Collectively, AAV6-M2 successfully delivered
276 CD19 CAR into the human T cells *in vivo*, which can be detected in the peripheral blood
277 two weeks post-AAV injection, and effectively depleted both circulating and tissue-
278 resident B cells.

279 To assess the differentiation state within CAR⁺ CD8⁺ T cells *in vivo*, we analyzed Tn, TCM,
280 TEM, and terminally differentiated effector memory re-expressing CD45RA (TEMRA)
281 subsets across tissues. CAR⁺ CD8⁺ T cells were predominantly of TEM phenotype, while
282 Tn and TCM subsets were minimally detected in these tissues (**Figure 4G**,
283 **Supplementary Figure 4F-I**). Given our *in vitro* data showing that Tn and TCM cells
284 adopt a TEM phenotype following AAV-CAR transduction and antigen encounter
285 (**Supplementary Figure 3H-J**), the tissue-resident TEM cells observed *in vivo* are likely
286 derived from these early-stage subsets and reflect the active killing of human B cells.
287 Together, these findings suggest that the effective B cell depletion in the AAV6-M2-CAR
288 group is accompanied by a dominant presence of CAR⁺ CD8⁺ TEM cells.

289 Next, we examined the transduction specificity of AAV-M2 *in vivo*. Among various immune
290 cell types in tissues and blood, CD8⁺ T cells were preferentially converted to CAR-T cells
291 compared to CD4⁺ T cells. CAR⁺ cells were barely found in B cells, monocytes, and NK
292 cells (**Figure 4H**). As systemically injected AAV tends to accumulate in the liver, we also
293 examined the biodistribution of the AAV vector. Compared to the wild-type AAV6, the
294 engineered AAV6-M2 shows significant de-targeting from the liver and reduced viral
295 accumulation across all organs (**Figure 4I**). Furthermore, in cynomolgus macaque, AAV6-
296 M2 showed minimal biodistribution to peripheral tissues, with very low levels of viral

297 genomes detected, including in the liver (**Figure 4J**). Together, these findings
298 demonstrate that AAV6-M2 selectively targets human T cells while minimizing off-target
299 liver transduction in both humanized mice and non-human primates, supporting its
300 favorable safety profile for in vivo T cell engineering.

301

302 **AAV6-M2 ameliorated lupus pathologies in SLE HIS mice via B cell depletion**

303 To further evaluate the efficacy of *in vivo* generated CAR-T cells in a disease context, we
304 employed a systemic lupus erythematosus (SLE) HIS mouse model induced by topical
305 application of R848, a TLR7/8 agonist (**Figure 5A**). SLE HIS mice were randomly
306 assigned to SLE and SLE+AAV groups, with comparable levels of human CD45 cells,
307 human B cells, IgG, and anti-dsDNA antibody (**Supplementary Figure 5A-D**). Following
308 systemic administration of AAV6-M2-CAR at week 0, we monitored the B cell levels in
309 peripheral blood from week 2 to week 8. A rapid and sustained decline in circulating B
310 cells was observed in the SLE+AAV group beginning at week 2, with significantly lower B
311 cell levels compared to the untreated SLE group (**Figure 5B**).

312 To evaluate the tissue-wide impact of CAR-T activity beyond peripheral blood, we
313 quantified human B cells across multiple organs at the study endpoint. Flow cytometry
314 revealed a significant reduction in the percentages of human B cells in the spleen, bone
315 marrow, liver, lung, and kidney of the SLE+AAV group compared to the untreated SLE
316 group (**Supplementary Figure 5E**). Although the percentages of B cell reduction in the
317 bone marrow did not reach statistical significance due to an outlier, a clear downward
318 trend was observed, with significantly lower B cell counts detected in the AAV6-M2-
319 treated animals (**Figure 5C**). Subtype analysis further demonstrated that the depletion
320 encompassed all major B cell subsets, including transitional, naïve, memory B cells, and
321 plasmablast cells (**Supplementary Figure 5F**). Notably, transitional B cells, which
322 represent the majority of developing human B cells in bone marrow, were nearly
323 undetectable following AAV6-M2-CAR administration (**Supplementary Figure 5G**).
324 Naïve and memory B cells and plasmablast cells were also significantly reduced in the
325 bone marrow (**Supplementary Figure 5H-I**). In the spleen, we found a similar B cell count
326 depletion (**Figure 5D**) and a marked reduction of splenic plasmablast and plasma cells

327 (PB&PC), as evidenced by a significant drop in CD38⁺ CD138⁺ populations
328 (**Supplementary Figure 5K-L**), which are the primary source of autoantibody production
329 in SLE and contribute directly to immune complex deposition and tissue inflammation.
330 Together, bone marrow and spleen analysis inform the direct on-target activity of CAR-T
331 therapy, indicating systemic suppression of B cell development and differentiation.

332 Lupus nephritis (LN) is a major SLE complication associated with progression to renal
333 failure and an overall worse prognosis. In the kidney, the reduction of glomerular IgG
334 deposition in the SLE+AAV group indicated a marked alleviation of immune complex-
335 mediated damage and served as a critical readout for therapeutic efficacy (**Figure 5E**,
336 **Supplementary Figure 5M**). Consistent with this, circulating levels of anti-dsDNA and
337 anti-Smith (Sm) antibodies significantly declined following AAV treatment (**Figure 5F-G**),
338 and serum blood urea nitrogen (BUN) and creatinine (CREA) levels also significantly
339 reduced, indicating improved renal function (**Figure 5H-I**). In the lung, histological
340 analysis by H&E staining showed preserved alveolar architecture and reduced
341 inflammatory infiltration in the SLE+AAV group, in contrast to the mild to moderate
342 perivascular and interstitial inflammatory infiltrates observed in the SLE group (**Figure 5J**,
343 **Supplementary Figure 5O**). Flow cytometry confirmed the depletion of human B cells in
344 the lung, consistent with the observed histological improvement (**Supplementary Figure**
345 **5N**). In the liver, mild immune cell infiltration was present in the SLE group but completely
346 absent in the SLE+AAV group, aligning with the efficient clearance of tissue-resident B
347 cells (**Supplementary Figure 5P-Q**). Together, these data demonstrate that
348 administering AAV6-M2-CAR not only eliminates systemic and tissue-resident B cells but
349 also alleviates multi-organ inflammation and protects organ function in a humanized SLE
350 model.

351

352 **Discussion**

353 This study demonstrates that a clinically validated delivery platform, the recombinant AAV
354 vector, can be engineered to efficiently and specifically deliver transgenes into human T
355 both *in vitro* and *in vivo*. We showed that AAV6-M2, an engineered AAV6 variant,
356 successfully generates both transient and stable CAR-expressing T cells *in vitro*. Through

357 a combination of CRISPR screening, cryo-EM, and molecular docking, we identified
358 CD62L, a surface marker expressed on less-differentiated T cells, as a key facilitator of
359 AAV6-M2, but not AAV6-WT, entry into human T cells. This unique tropism enables AAV6-
360 M2 to deliver CD19 CAR into resting human T cells and trigger antigen-dependent
361 cytotoxicity upon encountering CD19⁺ NALM6 cells. *In vivo*, systemic administration of
362 AAV6-M2-CAR into HIS mice resulted in up to 85.2% of CAR⁺ CD8⁺ T cells six weeks
363 post-injection. In HIS SLE mice, human B cells were effectively depleted in both the
364 peripheral blood and organs, accompanied by improvements in lupus-associated
365 pathologies. Notably, AAV6-M2 exhibited striking liver detargeting, with viral genome
366 accumulation in the liver reduced by more than two orders of magnitude in both mouse
367 and cynomolgus macaque, compared to the wild-type AAV6 and AAV9.

368 While lentivirus, LNP, and VLP have been explored for *in vivo* T cell engineering, this
369 study is, to our knowledge, the first to demonstrate that systemic injection of a single AAV
370 vector can generate persistent and functional human CAR-T cells *in vivo*. Given that AAV
371 is used in eight FDA-approved gene therapies, this finding marks an advance in the
372 application of AAV vector for *in vivo* T cell engineering. Natural AAVs are known to
373 accumulate in the liver following intravenous injection. Therefore, achieving both liver
374 detargeting and T cell specificity is critical to bringing AAV into the realm of *in vivo* CAR-
375 T therapy. By changing amino acids in the VR VIII loop, which protrudes to the surface of
376 the AAV viral particle, AAV6-M2 exhibited strong tropism to human T cells while largely
377 escaping from the liver. CRISPR-based receptor screening and validation confirmed that
378 CD62L is required for AAV6-M2 transducing T cells, even without prior activation. The
379 CD62L surface marker decorated naïve and early-memory T cells with higher plasticity
380 and greater ability to proliferate, which are favored by CAR-T cell therapy.

381 Similar to the LNP, lentivirus (LV), and virus-like particle (VLP) platforms, our AAV-based
382 *in vivo* CAR-T system demonstrates proof-of-concept but still requires further optimization
383 through future biotechnological advancements. First, CAR sequences delivered as
384 episomal DNA are subject to dilution as T cells proliferate. Although robust CAR-T cell
385 signals were detected six weeks after AAV injection, site-specific CAR integration into the
386 T cell genome using CRISPR may further extend CAR expression and provide more

387 durable immune surveillance against target cells. Dual-AAV delivery represents a
388 potential strategy to balance the need for stable CAR expression with the risks associated
389 with random integration from lentiviral vectors. The differing kinetics of CAR-T cells
390 generated via LNP, AAV, or lentiviral approaches warrant detailed investigation, as they
391 likely dictate the most appropriate therapeutic indications for each platform. For example,
392 a single dose of our current AAV-based *in vivo* CAR-T was sufficient to clear human B
393 cells and ameliorate lupus-like pathology in HIS mice, whereas more persistent CAR-T
394 cells may be required to control tumor progression. Second, leveraging AAV as a delivery
395 platform to treat non-rare diseases, particularly tumors prone to relapse, offers exciting
396 opportunities while also revisiting the long-standing challenge of redosing. LNP has been
397 dosed repeatedly within a short interval (e.g., one week), boosting peripheral CAR-T cell
398 levels⁹. Encouragingly, anti-CD40-mAb and CD20×CD3 bispecific antibodies have been
399 used in non-human primates to suppress anti-AAV antibody response and enable repeat
400 administration²⁶. IgG degrading enzymes (e.g., Imlifidase) have also been actively
401 investigated in preclinical and clinical studies for prophylactic immunomodulation in *in*
402 *vivo* gene therapy, enabling AAV administration in the presence of pre-existing antibodies
403 or allowing for readministration in non-human primates²⁷. Whether such strategies can
404 similarly enhance the antigen-dependent cytotoxicity of AAV-delivered CAR-T cells
405 remains a promising direction for future investigation. Finally, the use of T-cell-specific,
406 compact, and potent promoters and enhancers may further enhance selective and robust
407 CAR expression in the desired cell types, thereby increasing the safety margin.

408 We demonstrate that an engineered AAV6 variant, exhibiting superior transduction
409 efficiency in human T cells and markedly reduced liver targeting, can deliver CAR
410 sequences via systematic administration and generate functional CAR-T cells *in vivo*.
411 This study establishes a novel *in vivo* CAR-T platform built upon a clinically validated and
412 widely used delivery vector. Moreover, it broadens the therapeutic potential of AAV-
413 mediated gene transfer beyond inherited disorders, extending into the treatment of
414 acquired and immune-related diseases.

415

416 **Methods**

417 AAV packaging

418 ITR-containing GOI plasmid was utilized for packaging with different AAV capsid plasmids
419 and adenovirus helper plasmid using polyethyleneimine (24765-1, Polysciences). To pack
420 AAV, HEK 293T cells were seeded in 150 mm plates; The GOI, capsid, and helper
421 plasmids were added at a ratio = 1:1:1 (**Supplementary Table 1**). After 72 hours, the
422 transfected HEK 293T cells were collected in SAN digestion buffer and lysed by three
423 rounds of rapid freeze/thawing, followed by a 1 h incubation at 37°C with 100 units/ml
424 Benzonase (20156ES60, Yeasen). AAV was further purified following cell harvest and
425 PEG precipitation using iodixanol (OptiPrep, #07820, StemCell Technologies) gradient
426 ultracentrifugation. The purified AAV was treated with DNasel (AM2238, Invitrogen) and
427 Proteinase K (W0013, Qiagen). The titer of AAV was determined by qPCR with ChamQ
428 Universal SYBR qPCR Master Mix (Q711, Vazyme) via LightCycler®96 (Roche). Relative
429 quantity was estimated compared to a serial dilution of a plasmid standard of known
430 concentration. Primers for AAV titration were listed in **Supplementary Table 2**.

431 For large-scale AAV preparation, AAV particles were produced in a 3-liter bioreactor
432 (Duoning) using WayneLVPro™ HEK293 cells (QUACELL) transfected with a three-
433 plasmid system at a 1:1:1 ratio (GOI: capsid: helper plasmid). At 72 hours post-
434 transfection, cells were harvested, and the AAV particles were purified by iodixanol
435 gradient ultracentrifugation, followed by concentration and buffer exchange using
436 tangential flow filtration (TFF). Final AAV products were resuspended in DPBS and stored
437 at 4 or -80 °C.

438 The quality of purified AAV was assessed through: (1) Purity analysis by SDS-PAGE
439 (SurePAGE, 4-20%, GenScript) with Coomassie Blue staining (GenScript); (2) Genomic
440 titer quantification via absolute qPCR using ChamQ Universal SYBR qPCR Master Mix
441 (Vazyme Q711) on a LightCycler® 96 System (Roche). Titers were calculated from a
442 standard curve generated by serial dilutions of linearized plasmid DNA containing the
443 transgene expression cassette (concentration verified by Nanodrop™). (3) Ratio of
444 full/empty capsid was determined by analytical ultracentrifugation (Beckman Optima AUC
445 A/I, An-50 Ti rotor, 20°C, 16,000 rpm).

446 Three GOIs were used in this study:

447 scAAV-EGFP: CAG-EGFP (in vitro experiments)

448 ssAAV-CD19CAR-EGFP: EF-1 α -CD19CAR-EGFP (in vitro and mouse experiments)²⁸

449 scAAV-EGFP-Barcode: CAG-EGFP-barcode (non-human primates experiments)

450

451 In vitro culture and transduction of primary cells and cell lines

452 • Human peripheral blood mononuclear cells (PBMCs) and primary T cells

453 Peripheral blood from healthy donors was obtained with informed consent and
454 institutional ethical approval from Liquan Hospital (Shanghai, China), Boren Hospital
455 (Beijing, China), and the Affiliated People's Hospital of Ningbo University (Ningbo, China).

456 PBMCs were isolated by density gradient centrifugation using Ficoll-Paque. Human
457 primary T cells were subsequently purified from PBMCs using the Pan T Cell Isolation Kit
458 (Miltenyi Biotec, 130-096-535) according to the manufacturer's instructions.

459 To conduct transduction in activated T cells, human T cells were activated using Enceeed™
460 T cell Activation reagent (L00899, Genescript) for 24h in RPMI 1640 supplemented with
461 10% FBS and IL-2 at 100U/mL (Jiangsu Kingsley Pharmaceutical Co., Ltd.). AAV vectors
462 were then added at the indicated MOIs. Cells were maintained in IL-2-containing medium
463 (100 U/ml) throughout the culture period.

464 To conduct transduction in cells without activation, human PBMCs and resting T cells
465 were cultured in RPMI 1640 medium supplemented with 10% fetal bovine serum (FBS),
466 human IL-7 (5 ng/mL), and IL-15 (100 U/mL). Throughout the culture period, the medium
467 was half changed every three days. To assess transduction efficiency in post-transduction
468 activated T cells, activated human T cells were cultured in RPMI 1640 with 10% FBS and
469 human IL-2 (100 U/mL) following activation. Cells were washed three times thoroughly at
470 designated time points to remove residual AAV.

471 EGFP and CAR expression was assessed by flow cytometry at designated time points
472 following AAV transduction. CAR expression were detected by Biotin-SP–Goat Anti-

473 Mouse IgG, F(ab')₂ fragment-specific antibody (#115-065-006, Jackson
474 ImmunoResearch), followed by PE-conjugated anti-biotin antibody (#409003, BioLegend).

475 • Jurkat cells

476 The Jurkat cells were purchased from ATCC (TIB-152) and cultured in RPMI1640 medium
477 with 10% FBS. To generate Jurkat-SpCas9 cells, parental Jurkat cells were transduced
478 with the LentiCas9-Blast vector (Addgene, 52962) and selected with 2 µg/mL blasticidin.
479 Monoclonal SpCas9-expressing lines were established by limited dilution and expanded
480 under continuous 0.5 µg/mL blasticidin selection.

481 • NALM6 cells

482 The NALM6 cell line was kindly provided by Dr. Xv Li's laboratory at Westlake University
483 and maintained in RPMI 1640 medium with 10% FBS. To generate luciferase-expressing
484 cells, NALM6 cells were transduced by a lentiviral vector encoding luciferase and a
485 hygromycin resistance gene. Stable luciferase-expressing clones were selected and
486 expanded in the presence of 50 µg/mL hygromycin.

487

488 Cytotoxicity assay of CAR-T cells

489 To evaluate CAR-T cytotoxicity, activated human T cells were transduced with AAV6-WT-
490 CAR or AAV6-M2-CAR at an MOI of 1×10^4 . At day 2 post-transduction, NALM6 cells
491 were co-cultured with transduced T cells at a 1:1 ratio (T cell:B cell, T:B). After 24 hours
492 of co-culture, cells were harvested and stained with anti-human CD45 and anti-human
493 CD19 antibodies to distinguish NALM6 cells from human T cells. Cytotoxicity was
494 calculated using the following formula:

495 Cytotoxicity (%) = $100 \times (CD19^{+}\% \text{ in non-AAV control} - CD19^{+}\% \text{ in AAV-transduced cells})$
496 / $CD19^{+}\% \text{ in non-AAV control}$.

497 To evaluate CAR-T cytotoxicity in resting human T cell subtypes, Central memory T cells
498 (TCM; CCR7⁺CD45RO⁺), effector memory T cells (TEM; CCR7⁻CD45RO⁺), and naïve T
499 cells (TN; CCR7⁺CD45RO⁻) were isolated from pre-cultured human T cells using

500 fluorescence-activated cell sortor (BD FACSaria Fusion) and maintained in RPMI 1640
501 medium supplemented with 10% FBS, IL-7 (5 ng/mL), and IL-15 (100 U/mL). Each subset
502 was transduced with recombinant AAV (AAV) at a MOI of 1×10^5 . At 24 hours post-
503 transduction, cells were washed three times with RPMI 1640 and co-cultured with NALM6
504 cells at a T:B ratio of 1:1. From that point forward, the percentages of NALM6 cells (CD45-
505 CD19⁺), TCM, TEM, Tn, and TEMRA (CCR7⁻CD45RO⁻) populations in each well were
506 assessed by flow cytometry every three days.

507

508 Serum blocking assay

509 Serum samples were collected from 36 healthy donors at Zhejiang Cancer Hospital. All
510 procedures, including serum collection and experimental assays, were conducted under
511 ethical approval from both Zhejiang Cancer Hospital and Westlake University. PBMC from
512 four donors were used in this experiment.

513 To assess the inhibition of AAV transduction by pre-existing neutralizing antibodies, serial
514 10-fold dilutions of human serum (prepared in RPMI 1640 supplemented with 2% FBS,
515 starting at 1:2.5) were prepared in an 8-tube strip and mixed with equal volumes of AAV6-
516 M2-EGFP or AAV6-WT-EGFP (diluted in RPMI 1640 + 2% FBS) in a U-bottom 96-well
517 plate. The virus-serum mixtures were incubated at 37°C with 5% CO₂ for 1 hour, resulting
518 in final serum dilutions ranging from 1:5 to 1:5000 across four serial dilution steps.

519 After incubation, 5×10^4 human PBMCs (Shanghai Maishun Biotechnology Co., Ltd.),
520 pre-activated via Enceed™ T cell Activation reagent (L00899, Genescript) and human IL-
521 2 for 24 hours, were added to each well. Each well contained a final volume of 200 μ L
522 RPMI 1640 with 2% FBS and 100 U/mL IL-2. AAVs were added at an MOI of 5×10^3 .
523 Positive control wells contained AAV without serum, and negative control wells contained
524 neither AAV nor serum.

525 At 48 hours post-transduction, cells were stained with anti-human CD45 (BioLegend,
526 #304012) and anti-human CD3 (BioLegend, #317308), and EGFP expression in
527 CD3⁺CD45⁺ T cells was analyzed by flow cytometry. The EGFP⁺ percentage was
528 normalized using the formula:

529 (Sample EGFP% – Negative Control EGFP%) / (Positive Control EGFP% – Negative
530 Control EGFP%) × 100%.

531 Donors were grouped based on the highest dilution factor at which the EGFP⁺ percentage
532 dropped below 50%, and the number of donors in each group was plotted for AAV6-WT
533 and AAV6-M2, respectively.

534

535 Site-specific CAR insertion

536 The first AAV vector packaged sequences that encode CD19 CAR linked to tagBFP, with
537 the two expression cassettes connected by a self-cleaving T2A sequence. The CD19
538 CAR cassette was flanked by two 400-bp homology arms corresponding to the insertion
539 sites generated by a CRISPR system delivered by the second AAV. The second AAV
540 vector packaged sequences encoding an engineered AsCas12f-HKRA (enAsCas12f-
541 HKRA), a nuclear localization signal (NLS), EGFP, T2A, and an sgRNA targeting the first
542 exon of *TRAC*.

543 The dual AAV vectors were co-transduced into activated human T cells at an MOI 1×10⁵.
544 Transduced cells were cultured in RPMI 1640 medium supplemented with 10% FBS and
545 100 U/mL IL-2. The percentages of GFP⁺ and BFP⁺ cells were monitored by flow
546 cytometry post-transduction. Cells were also stained with anti-TCR α/β (#306727,
547 Biolegend) to assess TCR knockout, and the CAR expression was evaluated by Biotin-SP–
548 Goat Anti-Mouse IgG, F(ab')₂ fragment-specific antibody (#115-065-006, Jackson
549 ImmunoResearch), followed by PE-conjugated anti-biotin antibody (#409003, BioLegend).
550 Stable CAR⁺ T cells were defined as TCR[–] CAR⁺ cells.

551 Genomic insertion of the CAR sequence was verified by PCR amplifying the flanking
552 regions surrounding the insertion sites.

553

554 Genome-wide CRISPR/Cas9 screening

555 • Prepare lentivirus Brunello library

556 The transfer plasmid (LentiGuide-Brunello-mKate2), the pMD2.G (Addgene, 12259)
557 envelope plasmid, and the psPAX2 (Addgene, 12260) packaging plasmid were mixed at
558 the mass ratio 5:2:3 and incubated for 15 mins at room temperature. The mixture was
559 dropped to HEK293T cells at 80% confluency. Lentiviral supernatant was collected at 48
560 and 72 h post-transfection, filtered through a 0.45 μ m filter (Millipore, SLHV033RB), and
561 then concentrated by ultracentrifuging at 70,000g at 4°C for 2 h. Finally, the concentrated
562 lentivirus was aliquoted and stored at -80°C.

563 • CRISPR/Cas9 screening in Jurkat-Cas9 cells

564 LentiGuide-Brunello-mKate2 was transduced in Jurkat with stable Cas9 expression
565 (Jurkat-Cas9). The screening was performed in two Jurkat-Cas9 mono clones. For each
566 replicate, 7×10^7 Cas9-expressing Jurkat cells (~300X coverage) were transduced with
567 the lentiviral library at MOI ≤ 0.3 by infection and incubated overnight. Flow cytometry
568 confirmed transduction efficiencies at around 30% in each replicate for mKate2+/%
569 expression at 72h after lentivirus transduction. Cas9-expressing Jurkat cells (Jurkat-Cas9)
570 were selected and expanded in a culture medium with puromycin. When mKate2+/%
571 achieved above 95%, 10×10^7 cells per replicate were transduced with AAV6-WT-EGFP
572 or AAV-M-EGFP at the indicated MOI to allow the percentage of EGFP+ cells reached \geq
573 80%. At 72 h after AAV transduction, cells collected for the top 20% and bottom 20% were
574 sorted via Flow Cytometer. BD FACSAria™ Fusion and SONY MA900 were used for cell
575 sorting.

576 After sorting, genomic DNA was extracted by TIANamp Genomic DNA Kit (TIANGEN,
577 DP304-03). Then, sgRNA sequences were amplified using Q5 master mix (2 \times) (NEB
578 #M0544S) and purified using SPRI beads (Beckman #A63882) for NGS. PCR primers
579 with P5 and P7 adapters (NGS-Lib-KO-F and NGS-Lib-KO-R) were listed in
580 **Supplementary Table 2**. sgRNA sequences used in validation were listed in
581 **Supplementary Table 4**.

582 • Screening data analysis

583 The CRISPR screening was analyzed using MAGeCK²⁹. The difference in genes between
584 the bottom 20% of cells and the top 20% of cells was evaluated by the reads count of

585 corresponding gRNAs. In addition, the negative gRNAs were input as background with
586 parameter (--control-sgrna). The MAGeCK score and \log_2 fold change were used to rank
587 genes from the CRISPR screening. The \log_2 fold change was calculated as the \log_2
588 transformed ratio between the normalized read counts in the bottom 20% sample and the
589 top 20% sample. Normalization was based on the sequencing depth of each sample.

590 • Validating candidate genes in Jurkat cells

591 Candidate gene-knockout cell lines were generated using Jurkat-Cas9 cells transduced
592 with lentivirus encoding the indicated sgRNA under the U6 promoter. SgRNAs were
593 synthesized by GenScript (**Supplementary Table 4**). From day 2 after lentivirus
594 transduction, Jurkat cells were selected with puromycin (2 μ g/mL) for 7-10 days. Then,
595 the genomic DNA of the Jurkat cells was extracted for PCR amplification of the target
596 gene sequence. The indel% of the target gene was assessed via SYNTESGO analysis
597 based on Sanger sequencing of PCR products. Primers used in Sanger sequencing for
598 KO validation were listed in **Supplementary Table 2**. A total of 1×10^5 Jurkat-Cas9 cells
599 were transduced with AAV6-WT-EGFP or AAV6-M2-EGFP. Seventy-two hours after AAV
600 transduction, cells were collected and tested for EGFP expression via flow cytometry.

601 • Validating candidate genes in human T cells

602 Following 24 hours of activation, human T cells were nucleofected using the P3 Primary
603 Cell 4D-Nucleofector™ X Kit (Lonza, #V4XP-3032) and a 4D-Nucleofector™ X Unit
604 (Lonza, #AAF-1003X). Ribonucleoprotein (RNP) complexes were prepared by incubating
605 30 pmol of recombinant Cas9 protein (Takara, #632641) with 75 pmol of sgRNA at 25 °C
606 for 10 minutes. A total of 1×10^6 activated T cells were electroporated with RNPs per well
607 using the EO-115 program. After nucleofection, cells were resuspended in fresh culture
608 medium supplemented with cytokines. Three days post-knockout, AAV6-WT-EGFP or
609 AAV6-M2-EGFP were added to the culture at an MOI of 1×10^4 . Another three days later
610 (day 6 post-nucleofection), cells were collected and stained with anti-CD62L antibody.
611 EGFP expression was analyzed by flow cytometry in both CD62L⁺ and CD62L⁻ T cell
612 populations.

614 Cryo-EM structure

615 For cryo-EM sample preparation, 3.5 μ L of the AAV sample (1.3×10^{14} vg/mL) was applied
616 to a glow-discharged Quantifoil R1.2/1.3 Cu 300 mesh grid. Grids were blotted for 4 s with
617 a blot force of 10 following a 6 s waiting time using a Vitrobot Mark IV (Thermo Fisher
618 Scientific) under 100% humidity at 4 °C. The grids were then plunge-frozen in liquid
619 ethane cooled by liquid nitrogen.

620 Data collection was performed on a Titan Krios transmission electron microscope
621 (Thermo Fisher Scientific) operating at 300 kV, equipped with a Gatan K3 Summit direct
622 electron detector and a GIF Quantum energy filter (20 eV slit width). Movie stacks were
623 recorded in super-resolution mode at a nominal magnification of 130,000 \times using EPU
624 software, with a preset defocus range of -1.4 to -2.0 μ m in Aberration-Free Image Shift
625 (AFIS) mode. Each stack was exposed for 0.85 s (32 frames, 0.0266 s per frame), with a
626 total electron dose of \sim 50 e $^-$ / \AA^2 .

627 A total of 11,707 movie stacks were collected. Of these, 9,621 micrographs were manually
628 selected and processed using CryoSPARC v4.6.2. Patch motion correction and Patch
629 CTF estimation were applied. An initial round of auto-picking yielded \sim 157,235 particles
630 with a box size of 640 pixels. After iterative rounds of template-based particle picking and
631 2D classification, 156,281 particles were selected for ab initio reconstruction (C1
632 symmetry). Homogeneous refinement, followed by local CTF refinement and non-uniform
633 refinement, produced a final 3D reconstruction at an overall resolution of 1.8 \AA .

634 A structural model of AAV6-M2 was initially generated using the AlphaFold3 prediction³⁰.
635 Manual model adjustment and refinement were performed in COOT³¹, followed by atomic-
636 level refinement using Phenix³². Structural figures were prepared using ChimeraX³³.

637

638 Receptor docking

639 Flexible docking between AAV6-M2 and the transmembrane receptor L-selectin was
640 performed using the HADDOCK2.4 web server³⁴. The input structures included the AAV6-
641 M2 trimer and the lectin/EGF domains of L-selectin (PDB: 5VC1). All small molecules

642 were removed from the L-selectin structure, except for the calcium ion. The engineered
643 loop region of one AAV6-M2 monomer and the EGF domain of L-selectin were defined as
644 active residues for docking. The top-ranked docking model was visualized using
645 ChimeraX³⁵.

646

647 **Mouse experiments**

648 • HIS mice generation

649 NOD/ShiLtJGpt-Prkdc^{em26Cd52} II2rg^{em26Cd22} kit^{em1Cin(V831M)} II15^{em1Cin(hIL15)}/Gpt (NCG-X-hIL15)
650 mice (Strain NO. T037155) and NOD/ShiLtJGpt-Prkdc^{em26Cd52} II2rg^{em26Cd22}
651 Rosa26^{em1Cin(hCSF2&IL3&KITLG)}/Gpt (NCG-M) mice (Strain NO. T036669) were purchased
652 from GemPharmatech Co., Nanjing, China. These mice were housed under specific
653 pathogen-free (SPF) conditions at the Model Animal Research Center, Medical School of
654 Nanjing University, with all experiments conducted in compliance with institutional
655 guidelines under an approved animal protocol (LY-02). HIS mice were generated as
656 previously described³⁶. Briefly, human hematopoietic stem and progenitor cells (HSPCs)
657 were purified from fetal liver using the human CD34 MicroBead Kit (Miltenyi Biotec, 130-
658 046-702) following ethical approval (Drum Tower Hospital, protocol #2021-488-01/02).
659 Newborn NCG-M mice received 80 cGy sublethal irradiation followed by intrahepatic
660 injection of 5×10^4 CD34⁺CD38⁻ HSCs within 4-6 days after birth, whereas non-irradiated
661 NCG-X-hIL15 mice underwent the same HSC transplantation procedure. Successful
662 immune reconstitution was confirmed at 10 weeks post-engraftment by flow cytometry
663 detection of human immune cells (CD45⁺, CD3⁺, CD19⁺, CD14⁺, CD56⁺) in peripheral
664 blood, with engraftment defined as $>1 \times 10^5$ human CD45⁺ cells/mL.

665 • In vivo CAR-T generation in HIS mice

666 Humanized NCG-X-hIL15 mice demonstrating sufficient T cell engraftment ($\geq 15\%$ human
667 CD3⁺ T cells in peripheral blood human CD45⁺ cells) were randomly assigned to two
668 experimental groups. These groups received intravenous administration of either AAV-
669 M2-CAR19-EGFP or AAV6-CAR19-EGFP at a dose of 3×10^{13} vg/kg. Peripheral blood
670 CART signal and B cell dynamics were monitored at bi-weekly intervals via flow cytometry.

671 Mice were sacrificed 4 weeks and 6 weeks post-AAV injection for comparative immune
672 cells profiling in indicated tissues, including CAR-T cell transduction efficiency (EGFP⁺ in
673 human CD3⁺ T, CD4⁺ T, CD8⁺ T, Tn, TCM, TEM, TEMRA) and B cell depletion. Flow
674 cytometry (Agilent NovoCyte Penteon, Santa Clara, USA) was used for cell population
675 detection. Antibodies were listed in **Supplementary Table 3**. Gating strategies were
676 summarized in **Supplementary Figure 6A**.

677 • Evaluation of lupus pathologies in AAV6-M2-CD19CAR-treated HIS SLE mice

678 Humanized SLE (HIS-SLE) mouse model was generated as previously described (In
679 submission). Briefly, we topically administered the TLR7/8 agonist R848 to NCG-M
680 humanized immune system (HIS) mice for eight consecutive weeks to induce systemic
681 lupus-like manifestations. Following five weeks of R848 treatment, mice demonstrated
682 comparable levels of human immune reconstitution (quantified by peripheral blood human
683 CD45⁺ cell counts) and elevated serum autoantibody titers (quantified by anti-dsDNA
684 antibody) were randomly allocated to receive either AAV6-M2-CD19CAR (3×10^{13} vg/kg,
685 i.v.) or PBS control. Mice were euthanized at 8 weeks post-AAV administration for
686 endpoint analysis. Then, serum autoantibody levels were measured by ELISA: anti-
687 dsDNA antibody (COIBO BIO, CB13357-Hu) and anti-Sm antibody (COIBO BIO,
688 CB19966-Hu) following the manufacturer's instructions. Serum biochemical profiling was
689 quantified using an automated clinical analyzer (HITACHI 3500, Tokyo, Japan) following
690 manufacturer-recommended protocols. Subsequently, B cell subsets (Transitional B,
691 Naïve B, Plasmablast, Memory B) in indicated tissues were further analyzed by flow
692 cytometry. All antibodies used were listed in **Supplementary Table 3**. Gating strategies
693 were summarized in **Supplementary Figure 6B**.

694 • Quantification of AAV accumulation in the liver of HIS mice

695 Various organs from HIS mice were collected at the endpoint of the experiment. For each
696 organ, a 50-80 mg minced tissue sample was homogenized, and genomic DNA was
697 extracted using the TIANamp Genomic DNA Kit (TIANGEN, DP304-03). Absolute
698 quantification of AAV-delivered CAR copies was performed via qPCR using 100 ng of
699 gDNA per reaction. Primers (QCAR-F, QCAR-R) and probes (QCAR-Probe) targeting the

700 CAR transgene were designed as listed in **Supplementary Table 2**. PCR amplification
701 was conducted using Hot Start Taq 2× Master Mix (NEB #M0496S) with the following
702 thermocycling conditions: 95 °C for 30s, followed by 40 cycles of 95 °C for 15s, 52 °C for
703 30s, and 68 °C for 20s. Ct values were converted to AAV vector genome copies (Vg)
704 based on a standard curve.

705 • Quantification of AAV accumulation in the liver of B6 mice

706 C57BL/6J mice were purchased from the Animal Center of Westlake University and
707 housed under standard, individually ventilated, pathogen-free conditions at the
708 Laboratory Animal Resource Center of Westlake University. All animal experiments were
709 conducted in accordance with the Institutional Animal Care and Use Committee (IACUC)
710 guidelines approved by Westlake University. Six-week-old mice were administered AAV6-
711 WT-scEGFP, AAV6-M2-scEGFP, AAV6-Ark312-scEGFP, or AAV6-Ark315-scEGFP via
712 intravenous injection at a dose of 5×10^{12} vg/kg. Phosphate-buffered saline (PBS) was
713 injected intravenously as a negative control. At day 10 post-injection, mice were
714 euthanized, and livers were harvested for EGFP expression analysis using the PHOTON
715 IMAGER™ OPTIMA system, and EGFP signals from individual livers were quantified. The
716 AAV viral copies in the liver were also quantified by qPCR using a similar approach as
717 described in the HIS mice section. The capsid sequences of Ark312 and Ark315 were
718 obtained from published patents^{37,38}.

719

720 H&E staining

721 Liver and lung tissues were fixed in 4% paraformaldehyde (Beyotime Biotechnology,
722 P0099) at room temperature for 24 hours, dehydrated through a graded ethanol series,
723 cleared in xylene, and embedded in paraffin. Tissue sections were cut using a microtome,
724 mounted on glass slides, and dried overnight. For hematoxylin and eosin (H&E) staining,
725 sections were deparaffinized in xylene, rehydrated through a descending ethanol series
726 (100% to 70%), stained with Harris' hematoxylin for 3 minutes, and counterstained with
727 eosin Y for 1 minute. Slides were then dehydrated through an ascending ethanol series,

728 cleared in xylene, and coverslipped. Stained sections were examined using an Olympus
729 microscope (VS200, Olympus, Tokyo, Japan).

730

731 **Cynomolgus macaque experiments**

732 The non-human primate (NHP) experiments were conducted at the NHP facility of
733 InnoStar Biotechnology and approved by InnoStar's Institutional Animal Care and Use
734 Committee (IACUC). A 2-year-old cynomolgus macaque was used in this study. Four
735 weeks after intravenous administration of AAV (1×10^{12} vg/kg), the animal was euthanized
736 with 10 mg/kg ketamine hydrochloride and 5 mg/kg xylazine hydrochloride, followed by
737 PBS perfusion. To quantify viral genome copies, 50–100 mg of tissue samples were
738 homogenized in Buffer ATL (QIAGEN) using a tissue grinder. Genomic DNA and viral DNA
739 were extracted using the DNeasy Blood & Tissue Kit (QIAGEN) according to the
740 manufacturer's instructions. Vector genomes were amplified from the extracted DNA
741 using primers flanking the transgene and the Q5 High-Fidelity Master Mix (NEB
742 #M0544S). Amplicons containing Illumina adapter sequences were quantified using Qubit,
743 pooled at equal mass, and sequenced on an Illumina NovaSeq X Plus platform.

744

745 **Flow cytometry data collection and analysis**

746 Flow cytometry (Agilent NovoCyte Penteon and CytoFLEX) was used to analyze cells.
747 Flow cytometry data were analyzed via FlowJo.

748

749 **Statistical analysis**

750 Statistical analysis was performed using GraphPad Prism v8, and the specific tests were
751 indicated in the figure legend.

752

753 **References**

754 1 Baker, D. J., Arany, Z., Baur, J. A., Epstein, J. A. & June, C. H. CAR T therapy beyond
755 cancer: the evolution of a living drug. *Nature* **619**, 707-715, doi:10.1038/s41586-023-
756 06243-w (2023).

757 2 Maus, M. V. A decade of CAR T cell evolution. *Nat Cancer* **3**, 270-271,
758 doi:10.1038/s43018-022-00347-4 (2022).

759 3 Depil, S., Duchateau, P., Grupp, S. A., Mufti, G. & Poirot, L. 'Off-the-shelf' allogeneic
760 CAR T cells: development and challenges. *Nat Rev Drug Discov* **19**, 185-199,
761 doi:10.1038/s41573-019-0051-2 (2020).

762 4 Short, L., Holt, R. A., Cullis, P. R. & Evgin, L. Direct in vivo CAR T cell engineering.
763 *Trends Pharmacol Sci* **45**, 406-418, doi:10.1016/j.tips.2024.03.004 (2024).

764 5 Rurik, J. G. et al. CAR T cells produced in vivo to treat cardiac injury. *Science* **375**, 91-
765 96, doi:10.1126/science.abm0594 (2022).

766 6 Thomsen, G. et al. Biodistribution of onasemnogene abeparvovec DNA, mRNA and
767 SMN protein in human tissue. *Nat Med* **27**, 1701-1711, doi:10.1038/s41591-021-
768 01483-7 (2021).

769 7 Kheirolooom, A. et al. In situ T-cell transfection by anti-CD3-conjugated lipid
770 nanoparticles leads to T-cell activation, migration, and phenotypic shift. *Biomaterials*
771 **281**, 121339, doi:10.1016/j.biomaterials.2021.121339 (2022).

772 8 Billingsley, M. M. et al. In Vivo mRNA CAR T Cell Engineering via Targeted Ionizable
773 Lipid Nanoparticles with Extrahepatic Tropism. *Small* **20**, e2304378,
774 doi:10.1002/smll.202304378 (2024).

775 9 Hunter, T. L. et al. In vivo CAR T cell generation to treat cancer and autoimmune
776 disease. *Science* **388**, 1311-1317, doi:10.1126/science.ads8473 (2025).

777 10 Michels, A. et al. Lentiviral and adeno-associated vectors efficiently transduce
778 mouse T lymphocytes when targeted to murine CD8. *Mol Ther Methods Clin Dev* **23**,
779 334-347, doi:10.1016/j.omtm.2021.09.014 (2021).

780 11 Pfeiffer, A. et al. In vivo generation of human CD19-CAR T cells results in B-cell
781 depletion and signs of cytokine release syndrome. *EMBO Mol Med* **10**,
782 doi:10.15252/emmm.201809158 (2018).

783 12 Charitidis, F. T., Adabi, E., Thalheimer, F. B., Clarke, C. & Buchholz, C. J. Monitoring
784 CAR T cell generation with a CD8-targeted lentiviral vector by single-cell
785 transcriptomics. *Mol Ther Methods Clin Dev* **23**, 359-369,
786 doi:10.1016/j.omtm.2021.09.019 (2021).

787 13 Frank, A. M. et al. Combining T-cell-specific activation and in vivo gene delivery
788 through CD3-targeted lentiviral vectors. *Blood Adv* **4**, 5702-5715,
789 doi:10.1182/bloodadvances.2020002229 (2020).

790 14 Huckaby, J. T. et al. Bispecific binder redirected lentiviral vector enables in vivo
791 engineering of CAR-T cells. *J Immunother Cancer* **9**, doi:10.1136/jitc-2021-002737
792 (2021).

793 15 Andorko, J. I. et al. Targeted in vivo delivery of genetic medicines utilizing an
794 engineered lentiviral vector platform results in CAR T and NK cell generation. *Mol Ther*,
795 doi:10.1016/j.ymthe.2025.06.036 (2025).

796 16 Xu, J. et al. In-vivo B-cell maturation antigen CAR T-cell therapy for relapsed or
797 refractory multiple myeloma. *Lancet*, doi:10.1016/S0140-6736(25)01030-X (2025).

798 17 Banskota, S. *et al.* Engineered virus-like particles for efficient in vivo delivery of
799 therapeutic proteins. *Cell* **185**, 250-265 e216, doi:10.1016/j.cell.2021.12.021 (2022).

800 18 Hamilton, J. R. *et al.* Targeted delivery of CRISPR-Cas9 and transgenes enables
801 complex immune cell engineering. *Cell Rep* **35**, 109207,
802 doi:10.1016/j.celrep.2021.109207 (2021).

803 19 Hamilton, J. R. *et al.* In vivo human T cell engineering with enveloped delivery vehicles.
804 *Nat Biotechnol*, doi:10.1038/s41587-023-02085-z (2024).

805 20 Li, C. & Samulski, R. J. Engineering adeno-associated virus vectors for gene therapy.
806 *Nat Rev Genet* **21**, 255-272, doi:10.1038/s41576-019-0205-4 (2020).

807 21 Nyberg, W. A. *et al.* An evolved AAV variant enables efficient genetic engineering of
808 murine T cells. *Cell* **186**, 446-460 e419, doi:10.1016/j.cell.2022.12.022 (2023).

809 22 Nyberg, W. A. *et al.* In vivo engineering of murine T cells using the evolved adeno-
810 associated virus variant Ark313. *Immunity* **58**, 499-512 e497,
811 doi:10.1016/j.immuni.2025.01.009 (2025).

812 23 Arbones, M. L. *et al.* Lymphocyte homing and leukocyte rolling and migration are
813 impaired in L-selectin-deficient mice. *Immunity* **1**, 247-260, doi:10.1016/1074-
814 7613(94)90076-0 (1994).

815 24 Dhungel, B. P., Bailey, C. G. & Rasko, J. E. J. Journey to the Center of the Cell: Tracing
816 the Path of AAV Transduction. *Trends Mol Med* **27**, 172-184,
817 doi:10.1016/j.molmed.2020.09.010 (2021).

818 25 Kapitza, L. *et al.* CD62L as target receptor for specific gene delivery into less
819 differentiated human T lymphocytes. *Front Immunol* **14**, 1183698,
820 doi:10.3389/fimmu.2023.1183698 (2023).

821 26 Kyratsous, C. in *ASGCT2025*.

822 27 Leborgne, C. *et al.* IgG-cleaving endopeptidase enables in vivo gene therapy in the
823 presence of anti-AAV neutralizing antibodies. *Nat Med* **26**, 1096-1101,
824 doi:10.1038/s41591-020-0911-7 (2020).

825 28 Rodgers, D. T. *et al.* Switch-mediated activation and retargeting of CAR-T cells for B-
826 cell malignancies. *P Natl Acad Sci USA* **113**, E459-E468,
827 doi:10.1073/pnas.1524155113 (2016).

828 29 Li, W. *et al.* MAGeCK enables robust identification of essential genes from genome-
829 scale CRISPR/Cas9 knockout screens. *Genome Biol* **15**, 554, doi:10.1186/s13059-
830 014-0554-4 (2014).

831 30 Abramson, J. *et al.* Accurate structure prediction of biomolecular interactions with
832 AlphaFold 3. *Nature* **630**, 493-500, doi:10.1038/s41586-024-07487-w (2024).

833 31 Emsley, P., Lohkamp, B., Scott, W. G. & Cowtan, K. Features and development of Coot.
834 *Acta Crystallogr D Biol Crystallogr* **66**, 486-501, doi:10.1107/S0907444910007493
835 (2010).

836 32 Liebschner, D. *et al.* Macromolecular structure determination using X-rays, neutrons
837 and electrons: recent developments in Phenix. *Acta Crystallogr D Struct Biol* **75**, 861-
838 877, doi:10.1107/S2059798319011471 (2019).

839 33 Pettersen, E. F. *et al.* UCSF ChimeraX: Structure visualization for researchers,
840 educators, and developers. *Protein Sci* **30**, 70-82, doi:10.1002/pro.3943 (2021).

841 34 Honorato, R. V. et al. The HADDOCK2.4 web server for integrative modeling of
842 biomolecular complexes. *Nature Protocols* **19**, doi:10.1038/s41596-024-01011-0
843 (2024).
844 35 Pettersen, E. F. et al. UCSF ChimeraX: Structure visualization for researchers,
845 educators, and developers. *Protein Science* **30**, 70-82, doi:10.1002/pro.3943 (2021).
846 36 Ren, D., Liu, W., Ding, S. & Li, Y. Protocol for generating human immune system mice
847 and hydrodynamic injection to analyze human hematopoiesis *in vivo*. *STAR Protoc* **3**,
848 101217, doi:10.1016/j.xpro.2022.101217 (2022).
849 37 Eyquem, J., Nyberg, W. A., Asokan, A. & Ark, J. Adeno-associated virus compositions
850 and methods of use thereof for human cells. (2024).
851 38 Eyquem, J. & Nyberg, W. A. *In vivo* modification of cell genomes. (2024).
852

853 **Acknowledgments**

854 We thank the Biomedical Research Core Facilities, Laboratory Animal Resource Center,
855 and High-Performance Computer Center of Westlake University for their excellent
856 technical assistance. This work was supported by grants from the National Science
857 Foundation of China (32471533; 32471000; U24A20378), the Pioneer and Leading
858 Goose R&D Program of Zhejiang (grant no. 2024SSY0003), the Fundamental Research
859 Funds for the Central Universities (2024300408; XJ2024003602), the Research Center
860 for Industries of the Future (RCIF) at Westlake University, the National Science and
861 Technology Major Program (2023ZD0500400), National Natural Science Foundation of
862 China (32471000; U24A20378), and a Jiangsu Provincial Science and Technology Plan
863 Special Fund (BK20232018). This work was also partially supported by Westlake
864 Genetech.

865

866 **Author contributions**

867 L.M., Y.L., and Z.L. conceived the project and designed the experiments. L.M. and Z.L.
868 designed the capsid library. Y.L. designed the Human Immune System mouse model.
869 Q.S. and J.W. (Jing Wang) conducted AAV library preparation and screening with the
870 help of J.W. (Jiamei Wu) and Y. X.. K.N. and W.L. conducted CAR-T experiments *in vitro*
871 and *in vivo*, receptor CRISPR screening and validation with help from M.W., L.W., W.C.,
872 Y.C., R.Z., S.D., C.C. B.K., S.W., and X.Q.. Y.Z. and X.W. conducted cryo-EM

873 experiments with guidance from Y.W.. R.D. prepared AAV with help from the Westlake
874 Genetech CMC team. Z.L., R.Z., and H.C. conducted computational analysis and
875 molecular docking analysis with the help of Q.Z.. L.M., L.Z., K.N., Y.L., and W.L. wrote
876 the manuscript with input from all co-authors.

877

878 **Competing interests**

879 Westlake Genetech and Westlake University share intellectual property based on the
880 AAV variants of this study. Z.L. and L.M. are co-founders of Westlake Genetech. K.N.
881 was a postdoc in Lijia Ma's Lab at Westlake University when this project started. K.N.,
882 M.W., L.W., Q.Z., J.W., B.K., Y. X., S.W., G.W., M.D., and H.C. are currently full-time
883 employees of Westlake Genetech. Y.L. is currently consulting for GemPharmatech Co.

Figure 1 AAV6 variants show superior transduction efficiencies in human primary T cells

(A) A schema of AAV6-EGFP transduction in human primary T cells.

(B-D) The transduction efficiency was illustrated in a fluorescence histogram (B), percentage of EGFP+ cells (C), and mean fluorescence intensity (MFI) (D).

Figure 2 CD62L mediates enhanced transduction of AAV6-M2 in human T cells

(A) Schematic of the CRISPR screening strategy.

(B-C) Volcano plots of genome-wide CRISPR screen hits for AAV6-M2 (B) and AAV6-WT (C), showing MAGeCK score versus log-fold change (LFC). Top-ranked candidates, including *SELL* (CD62L), are highlighted.

(D) EGFP expression in Jurkat cells transduced with AAV6-M2 or AAV6-WT following AAVR knockout, CD62L knockout (two independent sgRNAs), or AAVR+CD62L double knockout. CD62L-negative cells were sorted in the analysis of CD62L knockout and AAVR+CD62L double knockout groups.

(E) Flow cytometry analysis of MFI of EGFP in CD62L⁺ and CD62L⁻ human primary T cells transduced with AAV6-M2 and AAV6-WT. Data collected from T cells of three donors and CD62L-knockout by two independent sgRNAs.

(F) Surface representation of the AAV6-M2 capsid resolved at 1.8 Å resolution by cryo-EM. The engineered VR IV loops are highlighted in yellow.

(G) Electrostatic surface potential map of the CD62L EGF domain (PDB: 5VC1), with the engineered VR IV loop of AAV6-M2 (yellow) docked into the binding pocket.

(H) Detailed view of the docking interface between the engineered VR VIII loop (yellow) and CD62L EGF domain (pink), showing residue-level interactions, including hydrogen bonds (dotted lines).

(I) Bar graph showing the distribution of the highest serum dilution titer against AAV6-WT and AAV6-M2 in human serum from 36 donors. Serum susceptibility is grouped by the highest dilution factor at which EGFP expression dropped below 50%.

Data shown as mean \pm SEM.; P values (D) were calculated by two-way ANOVA;
**** p \leq 0.0001; ns: not significant.

Figure 3 Efficient transduction and cytotoxicity of AAV6-M2-mediated CAR delivery in human T cells

(A) Time course of CAR expression in activated T cells (aT) from two donors after AAV6-M2-CAR transduction (MOI=5E4), measured by flow cytometry.

(B) Viability of aT cells after AAV6-M2-CAR transduction, compared to non-AAV controls.

(C) Schematic of the cytotoxicity assay setup, showing transduction, co-culture with NALM6 cells, and flow cytometry-based quantification of target cell killing.

(D) Cytotoxicity assay of AAV-CAR-transduced aT cells (MOI=1E4) co-cultured with NALM6 cells (T:B = 1:1). Cytotoxicity was assessed at multiple time points post co-culture.

(E) Construct design of the dual-AAV knock-in strategy targeting the *TRAC* locus: AAV vector 1 delivers the CAR-tagBFP cassette flanked by homology arms, and AAV vector 2 expresses sgRNA, enAsCAs12f, and EGFP.

(F-G) Quantification of cell populations over time by percentage (F) or cell numbers (G) after dual-AAV delivery in aT cells.

(H) Time course of EGFP expression in resting T cells (rT) transduced with AAV6-M2-EGFP, measured by flow cytometry.

(I) EGFP expression in rT cells post AAV6-M2 transduction followed by activation (Day 6).

(J) Experimental design for subtype-specific cytotoxicity assays. Human T cells were sorted into T naïve (Tn), central memory (TCM), and effector memory (TEM) subsets, transduced with AAV6-M2-CAR, and co-cultured with NALM6 cells.

(K) NALM6 cell abundance measured by flow cytometry over time following co-culture with Tn cells transduced with AAV6-M2-CAR.

Figure 4 In vivo CAR-T cell generation and B cell depletion by AAV6-M2 in humanized mice

(A) Schematic of the experimental timeline: HIS-NCGX-IL15 mice were intravenously injected with AAV6-WT-CAR or AAV6-M2-CAR (3×10^{13} vg/kg) and analyzed at 2 and 4 weeks post-injection.

(B-C) Flow cytometry analysis of CAR⁺CD3⁺ (B) and CAR⁺CD8⁺ (C) T cells in peripheral blood.

(D) Percentage of human B cells in various tissues following the administration of AAV6-WT-CAR or AAV6-M2-CAR.

(E-G) Tissue distribution of CAR⁺ cells in CD3⁺ (E), CD8⁺ (F), and CD8⁺ TEM (G) cells.

(H) Cellular phenotyping of CAR⁺ immune cells across tissues in AAV6-M2-CAR-treated mice.

(I) Biodistribution of vector genome copies in mouse organs quantified by qPCR.

(J) Relative vector genome copies in cynomolgus macaque organs quantified by NGS.

Each dot represents an animal. Data shown as mean \pm SEM.; P values (B-I) were calculated by Multiple unpaired t tests; * $p \leq 0.05$; ** $p \leq 0.01$; *** $p \leq 0.001$; **** $p \leq 0.0001$; ns: not significant.

Figure 5 AAV6-M2 in vivo CAR-T therapy eliminates B cells and ameliorates SLE symptoms in a humanized lupus model

(A) Experimental design. Humanized HIS-HCG-M mice were treated with R848 to induce SLE-like symptoms and injected with AAV6-M2-CAR. Tissues were collected at 8 weeks post-injection.

(B) Quantification of human B cells in peripheral blood over time.

(C-D) Total B cell counts in bone marrow (C) and spleen (D).

(E) Representative kidney immunofluorescence images showing human IgG deposition (pink) in the SLE group. Lower panels provide magnified views of the regions outlined by yellow rectangles in the corresponding upper panels.

(F–G) Serum levels of anti-dsDNA (F) and anti-Smith (Sm) autoantibodies (G).

(H–I) Levels of kidney injury markers BUN (H) and CREA (I).

(J) Representative lung histology showing alveolar inflammation in SLE and its reduction upon AAV6-M2 treatment.

Each dot represents an animal. Data shown as mean \pm SEM.; P values (B–D) were calculated by Mann-Whitney test; P values (F–I) were calculated by unpaired T tests.

* $p \leq 0.05$; ** $p \leq 0.01$; *** $p \leq 0.001$; **** $p \leq 0.0001$; ns: not significant.

Supplementary Figure 1 AAV6 variants show superior transduction efficiencies in human primary T cells

(A) An overview of the top AAV6 variants and wild-type AAV6 in the results of capsid screening.

(B) The packing efficiencies of AAV6-WT, AAV6-M1, and AAV6-M2 using adherent HEK 293T cells in a 15 cm plate.

(C) The packing efficiencies of AAV6-WT and AAV6-M2 using suspension HEK293 cells in a 3-liter bioreactor.

(D) AAV6-M2 capsid content determined by analytic ultracentrifugation (AUC) at wavelength 280 nm.

(E) Cropped view of a representative cryo-EM micrograph for AAV6-M2 sample.

Supplementary Figure 2 CD62L mediates enhanced transduction of AAV6-M2 in human T cells

(A) Volcano plots of genome-wide CRISPR screen hits for AAV6-M1, showing MAGeCK score versus log-fold change (LFC). Top-ranked candidates, including *SELL* (CD62L), are highlighted.

(B) Flow cytometry analysis of EGFP⁺ in CD62L⁺ and CD62L⁻ human primary T cells transduced with AAV6-M2 and AAV6-WT. Data collected from T cells of three donors and CD62L-knockout by two independent sgRNAs.

(C) Cryo-EM data processing workflow for AAV6-M2 capsid reconstruction.

(D) Cryo-EM structure of the AAV6-M2 monomer shown in two orientations rotated 180°, highlighting the engineered VRVIII loop in orange.

(E) Structural alignment of AAV6-WT (purple, PDB: 4V86) and AAV6-M2 (orange) VP3 monomers.

(F-G) Cryo-EM density maps (grey mesh) of the VRVIII loop fitted with atomic models from AAV6-M2 (F, yellow sticks) and AAV6-WT (G, purple sticks).

(H-I) Surface charges are displayed for AAV6-WT (H) and AAV6-M2 (I). blue: positive; red: negative.

(J) Schematic of serum susceptibility experiment.

Supplementary Figure 3 Efficient transduction and cytotoxicity of AAV6-M2-mediated CAR delivery in human T cells

(A) Schematic of AAV6-M2-CAR vector and experimental timeline for transducing activated human primary T cells (aT), followed by flow cytometry analysis.

(B) Expansion of aT cells from two donors after transduction with AAV6-M2-CAR or no-AAV control.

(C) Time course of NALM6 cell elimination in cytotoxicity assays using AAV6-M2-CAR or AAV6-WT-CAR transduced aT cells (T:B = 1:1).

(D) Schematic of AAV6-M2-EGFP transduction in resting human T cells (rT), followed by flow cytometry analysis.

(E) Schematic of AAV6-M2-EGFP transduction in resting human T cells (rT) then CD3/CD28 beads activation, followed by flow cytometry analysis.

(F-G) Cytotoxicity in TCM (F) and TEM (G) cells over time following AAV6-M2-CAR transduction and NALM6 co-culture.

(H-J) Composition of T cell subsets over time in Tn (H), TCM (I), and TEM (J) populations post co-culture with NALM6 cells.

Supplementary Figure 4 In vivo CAR-T cell generation and B cell depletion by AAV6-M2 in humanized mice

(A-B) Frequencies of B cells and T cells in peripheral blood prior to AAV injection show no differences between treatment groups.

(C-D) Longitudinal dynamics of B cells in peripheral blood over 4 weeks.

(E) CAR⁺ CD4⁺ T cell frequencies in mouse tissues following AAV6-M2-CAR and AAV6-WT-CAR administration.

(F-I) Subset analysis of CAR⁺ T cells across bone marrow (F), spleen (G), liver (H), and lung (I).

Each dot represents an animal. Data shown as mean \pm SEM; P values (A-B) were calculated by unpaired T tests; P values (C-I) were calculated by Multiple unpaired T tests.

* p \leq 0.05; ** p \leq 0.01; *** p \leq 0.001; **** p \leq 0.0001; ns: not significant.

Supplementary Figure 5 AAV6-M2 in vivo CAR-T therapy eliminates B cells and ameliorates SLE symptoms in a humanized lupus model

(A-D) hCD45⁺ cells (A), total IgG (B), B cell counts (C), and anti-dsDNA levels (D) in peripheral blood prior to AAV injection.

(E) Percentage of B cells among hCD45⁺ cells in multiple tissues.

(F) Composition of B cell subsets in bone marrow from one representative mouse.

(G–J) Quantification of transitional (G), naïve (H), memory (I), and plasmablast B cells (J) in bone marrow.

(K–L) Plasmablast and plasma cell (PB & PC) abundance in the spleen quantified by flow cytometry (L) and flow cytometry density plot (K).

(M) Representative kidney immunofluorescence images showing reduced human IgG deposition in AAV-treated mice. This plot is associated with Figure 5E.

(N–O) Quantification of B cells (N) and histological analysis (O) in the lung. This plot is associated with Figure 5J.

(P–Q) Quantification of B cells (P) and histological analysis (Q) in the liver. Yellow arrows indicate immune cells infiltrated into the liver.

Each dot represents an animal. Data shown as mean \pm s.d.; P values (A-D) were calculated by unpaired T tests; P values (E, G-J, N, and P) were calculated by Mann-Whitney tests.

* $p \leq 0.05$; ** $p \leq 0.01$; *** $p \leq 0.001$; **** $p \leq 0.0001$; ns: not significant.

Supplementary Figure 6 Gating strategies

(A) Gating strategy of the HIS mouse model.

(B) Gating strategy of the HIS SLE mouse model.

Figure 1

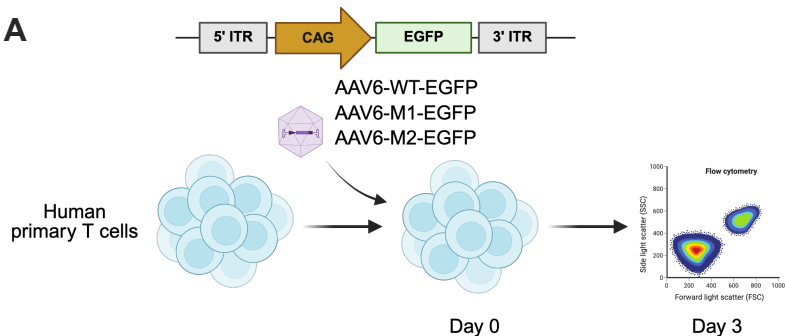
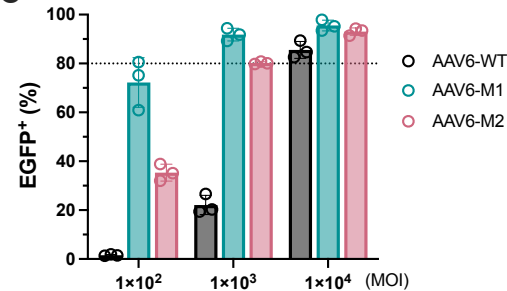
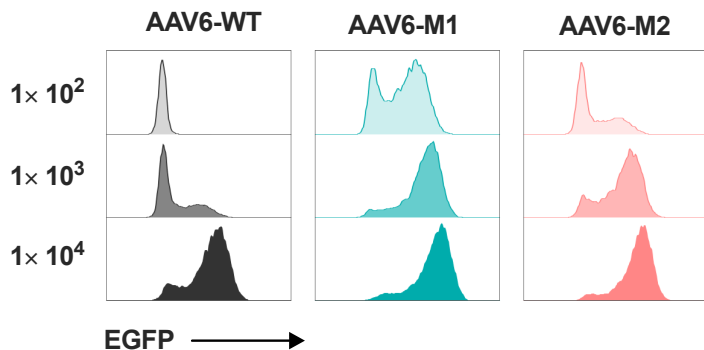
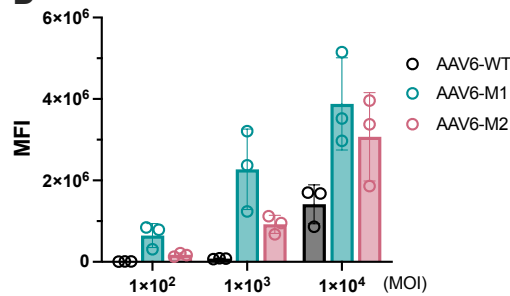
A**C****B****D**

Figure 2

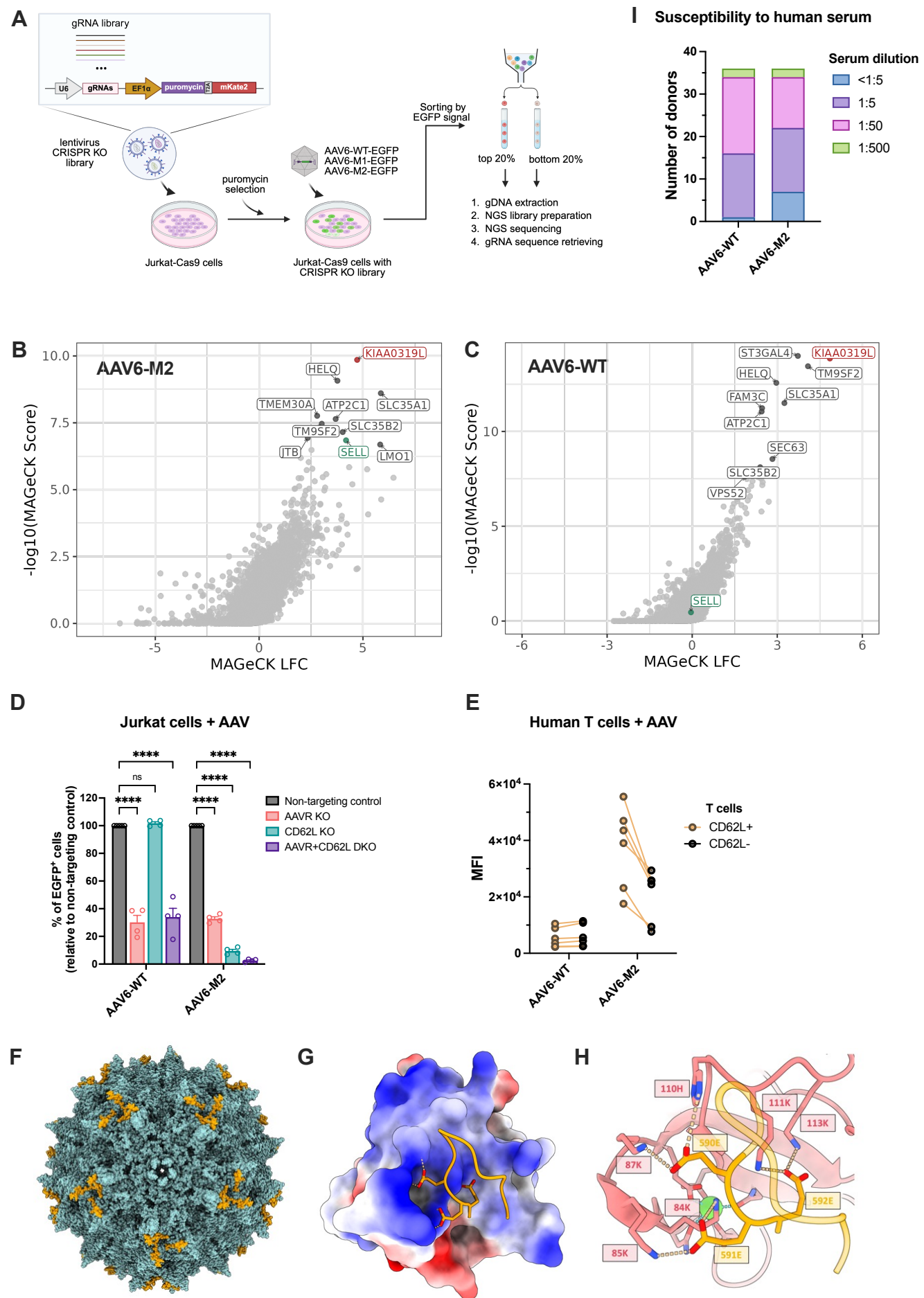


Figure 3

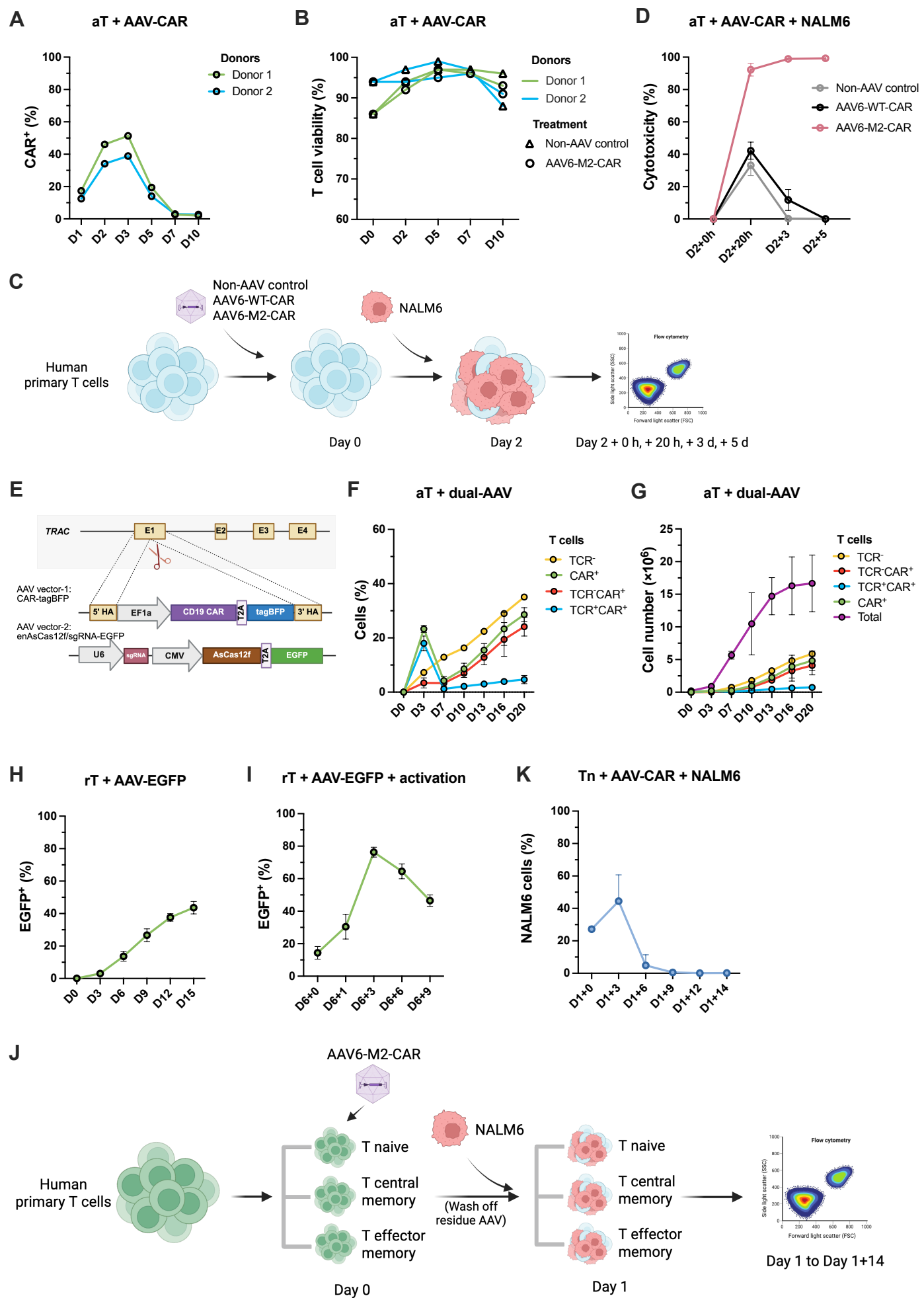
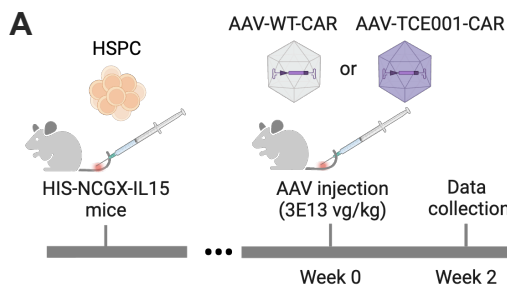
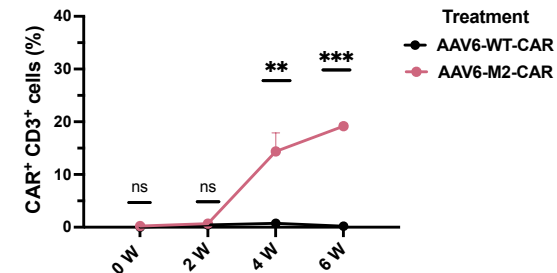


Figure 4

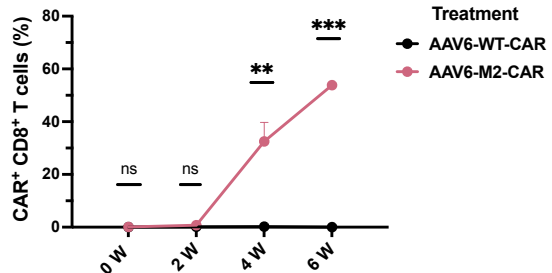


- Peripheral blood (PB)
- Spleen
- Bone marrow (BM)
- Liver
- Lung

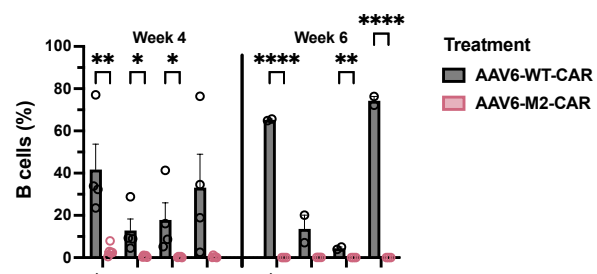
B Peripheral blood



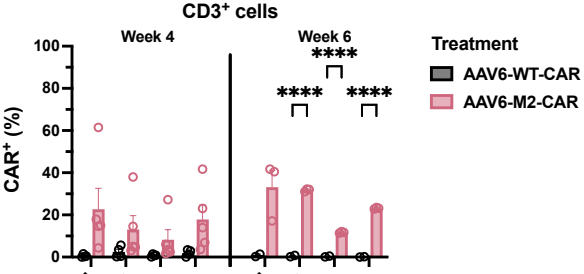
C Peripheral blood



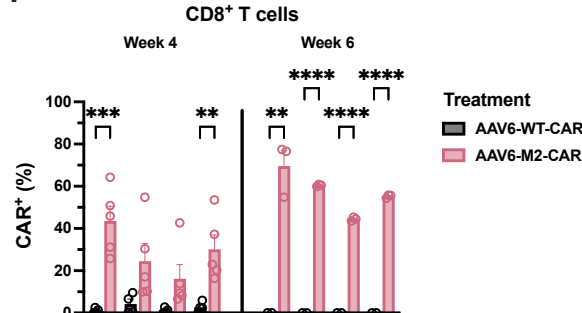
D hCD45⁺ cells



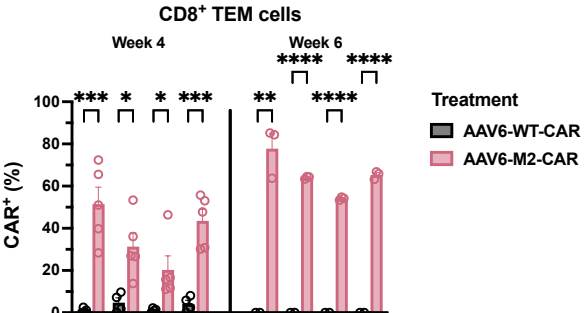
E CD3⁺ cells



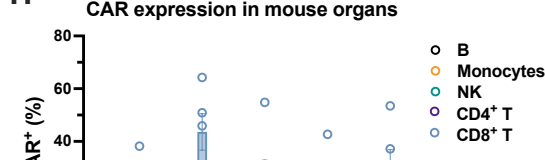
F CD8⁺ T cells



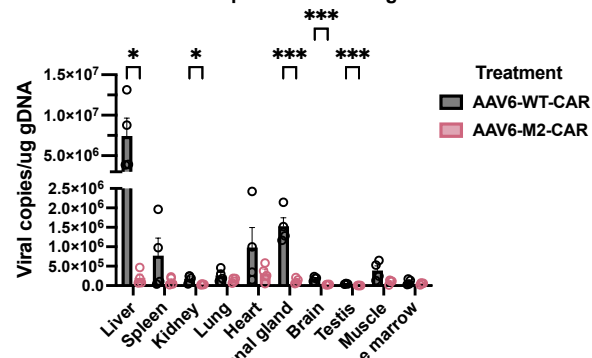
G CD8⁺ TEM cells



H CAR expression in mouse organs



I AAV viral copies in mouse organs



J AAV viral copies in cynomolgus macaque

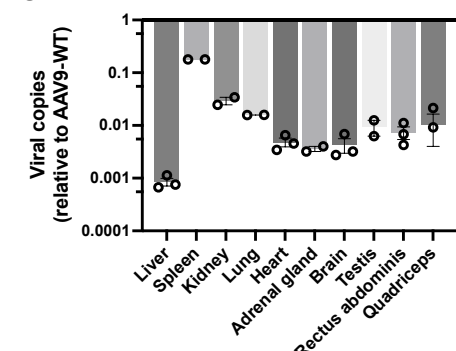
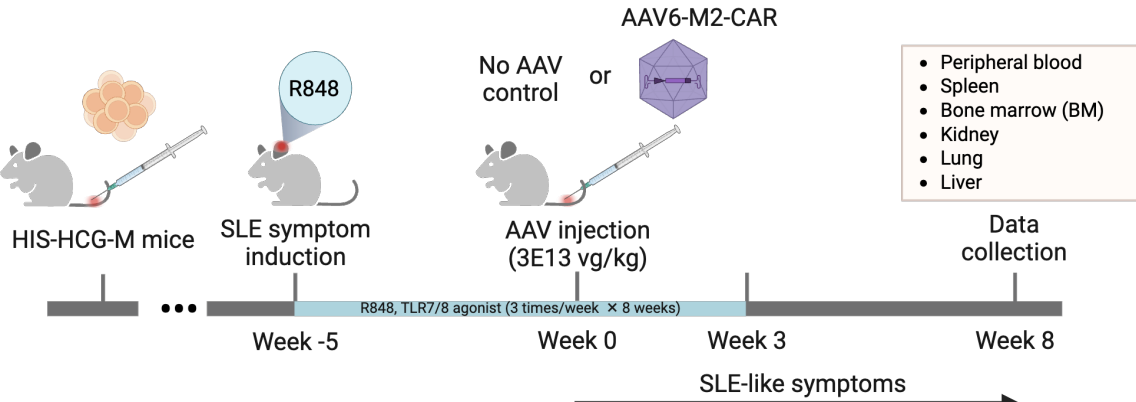
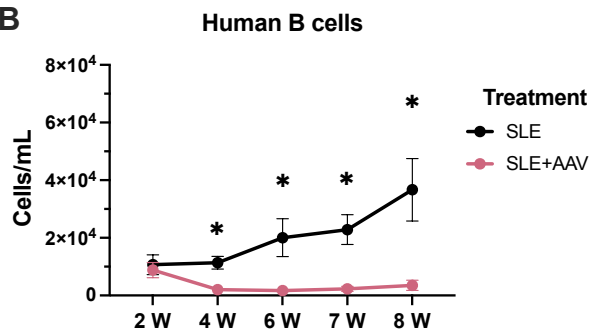


Figure 5

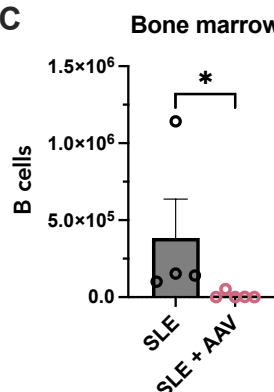
A



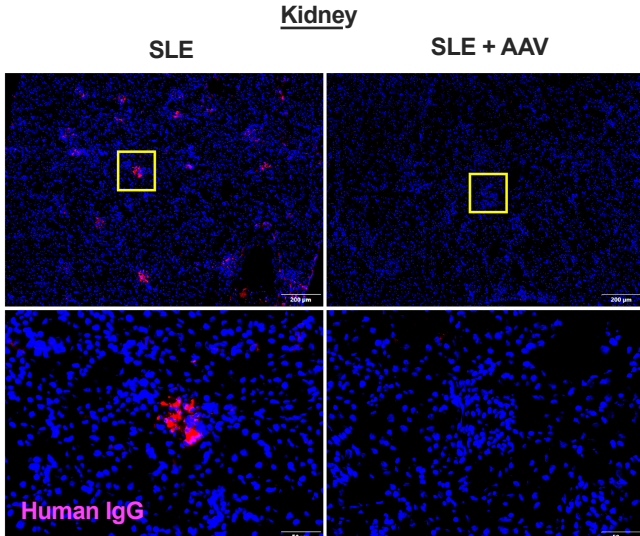
B



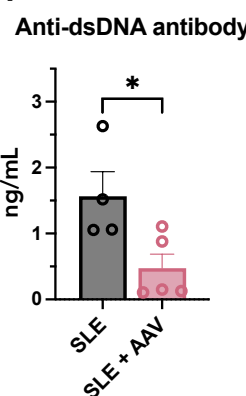
C



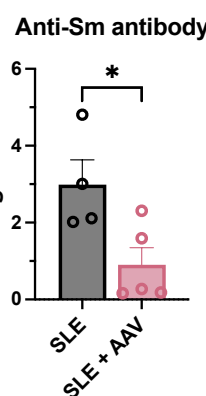
E



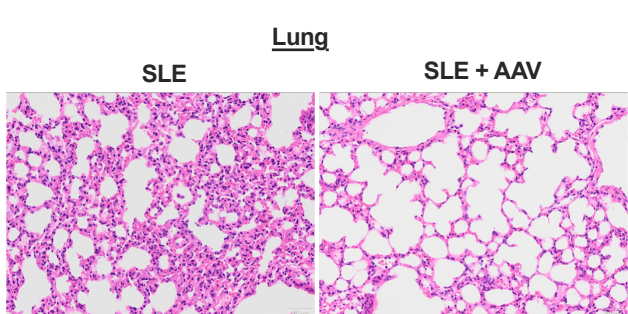
F



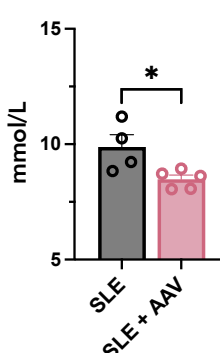
G



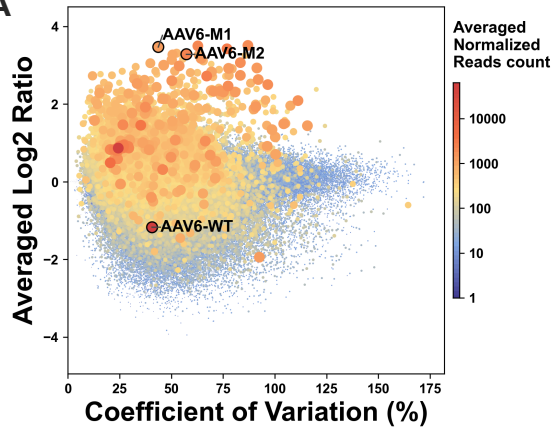
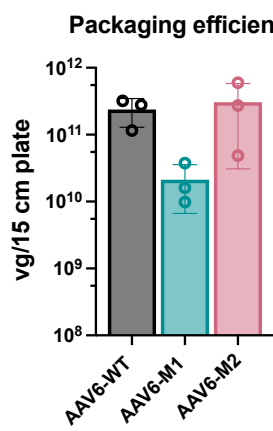
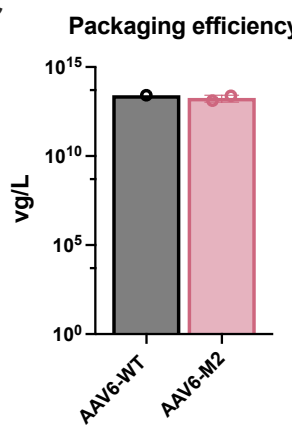
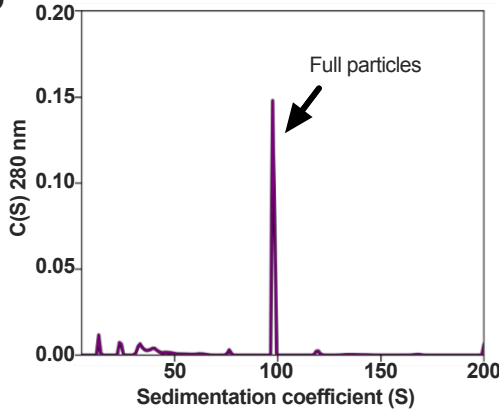
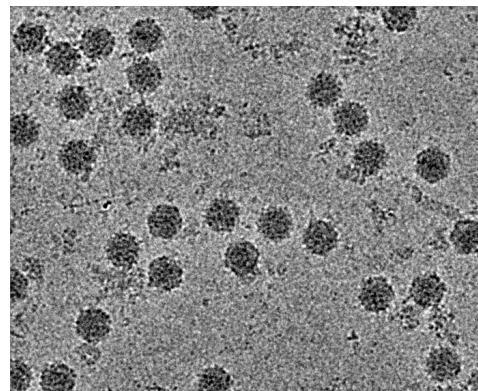
J



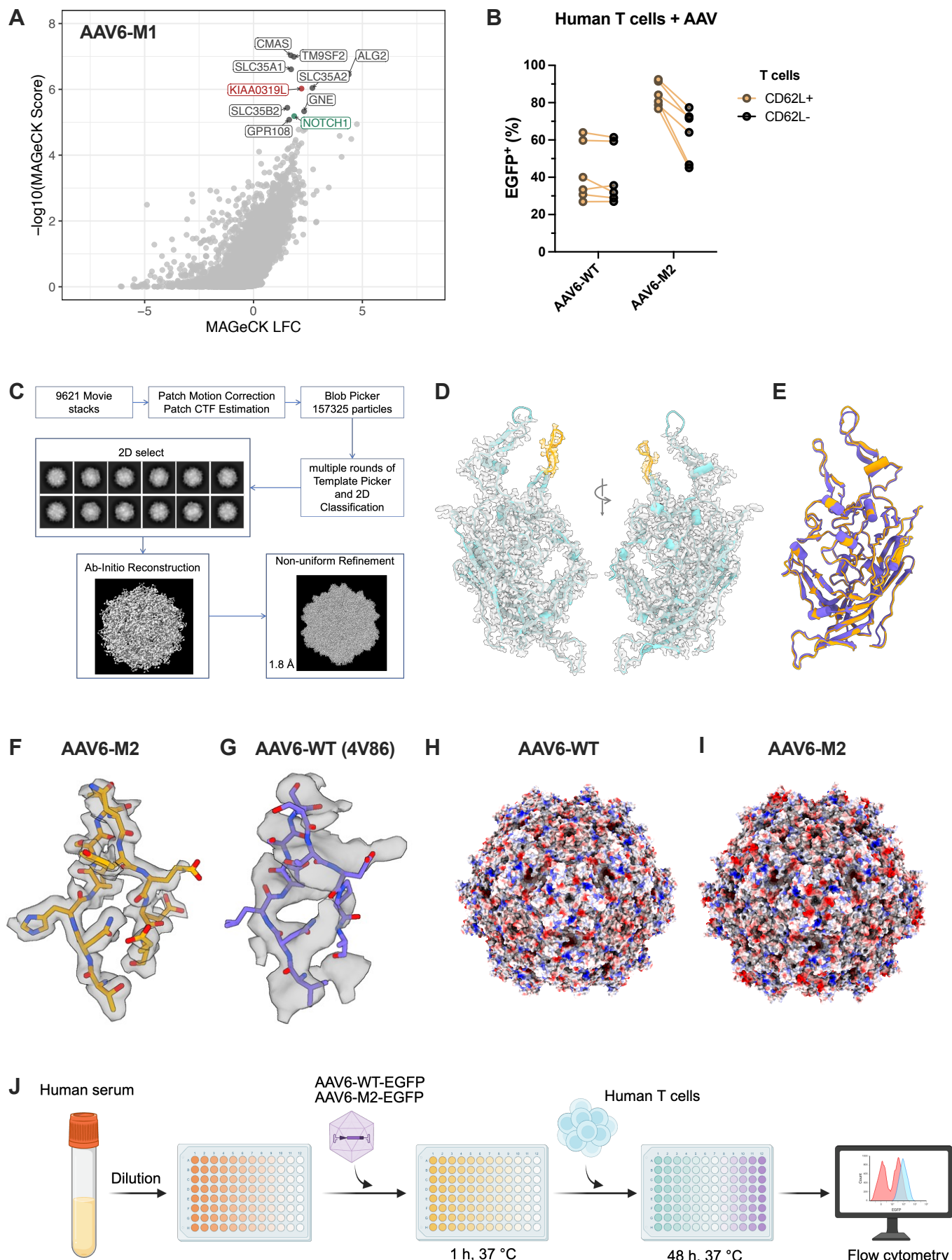
H



Supplementary Figure 1

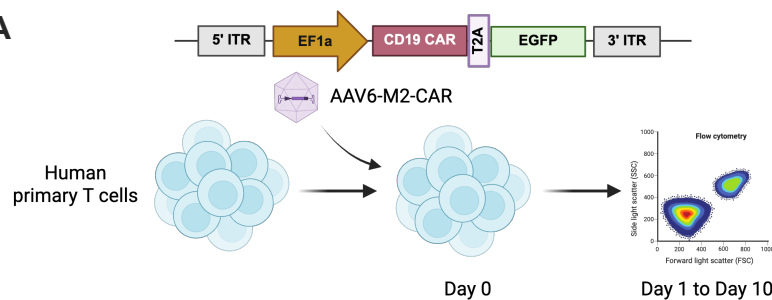
A**B****C****D****E**

Supplementary Figure 2

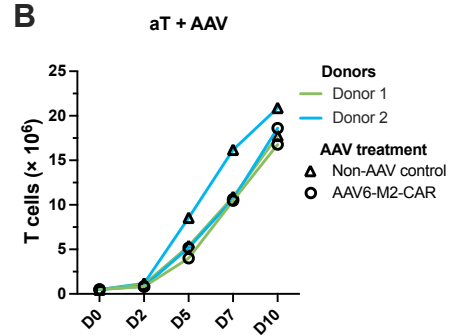


Supplementary Figure 3

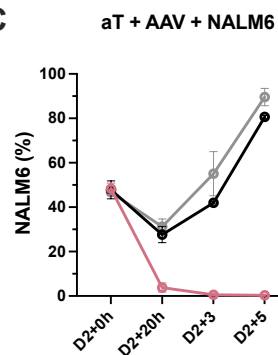
A



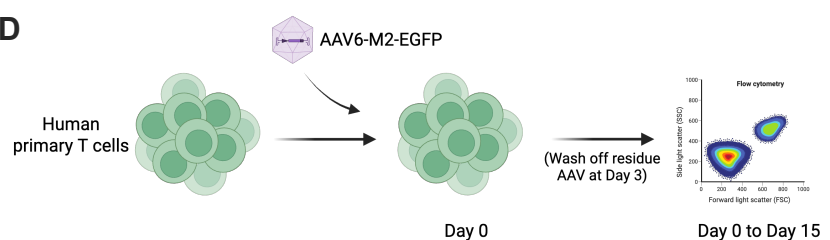
B



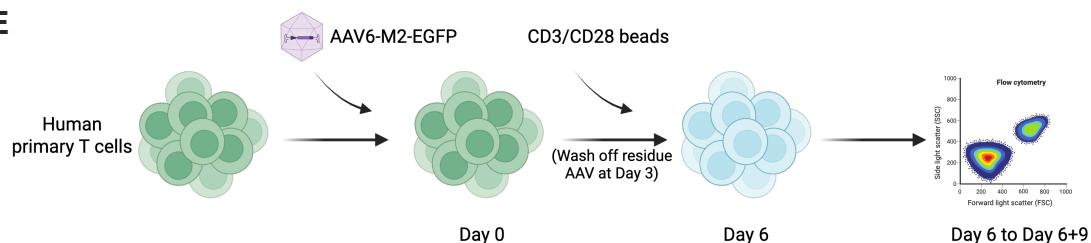
C



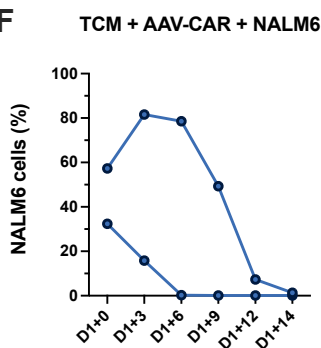
D



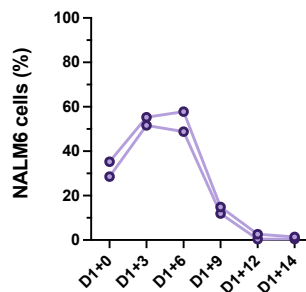
E



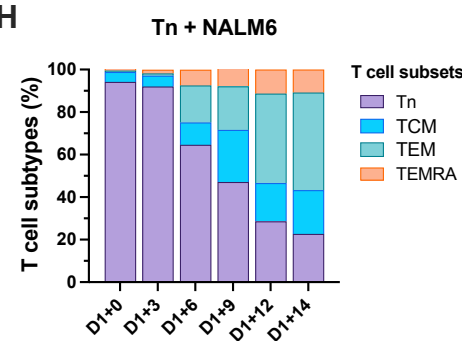
F



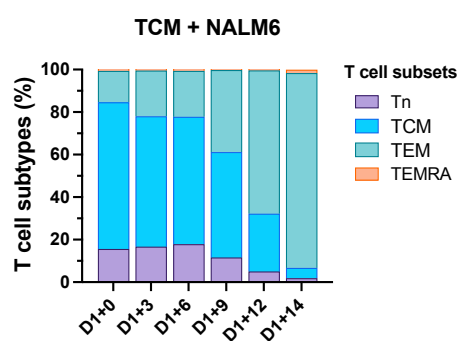
G TEM + AAV-CAR + NALM6



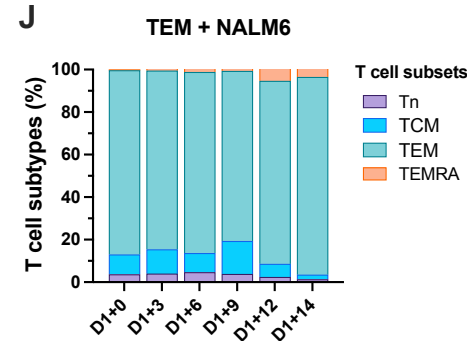
H



I TCM + NALM6

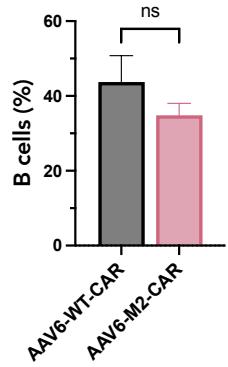


J

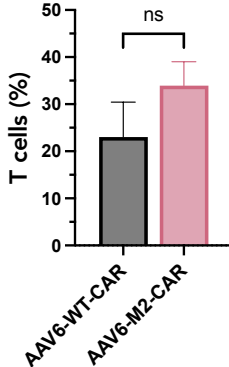


Supplementary Figure 4

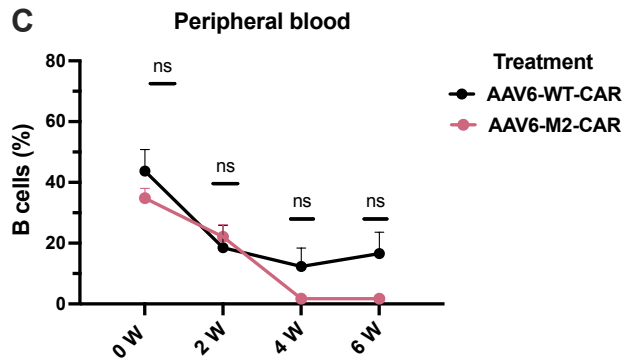
A



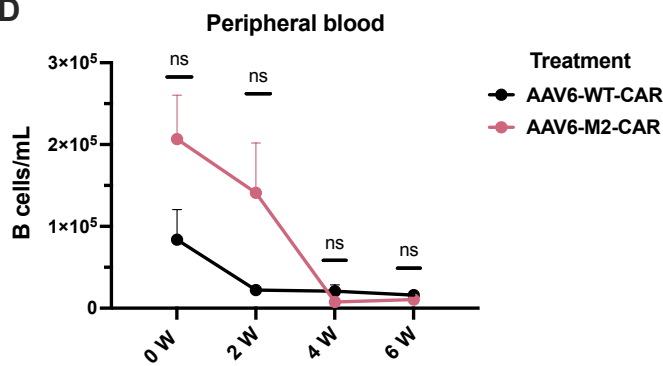
B



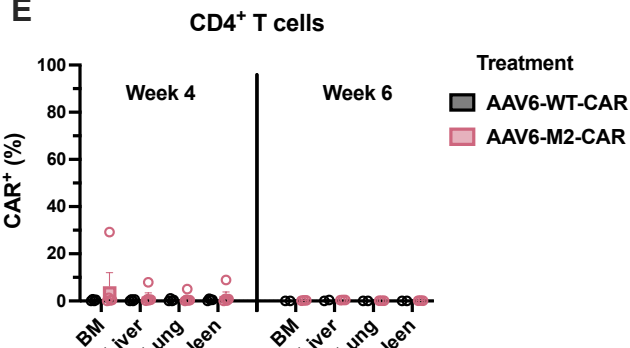
C



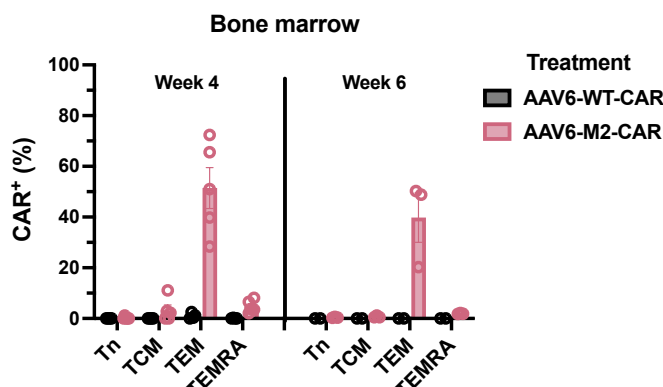
D



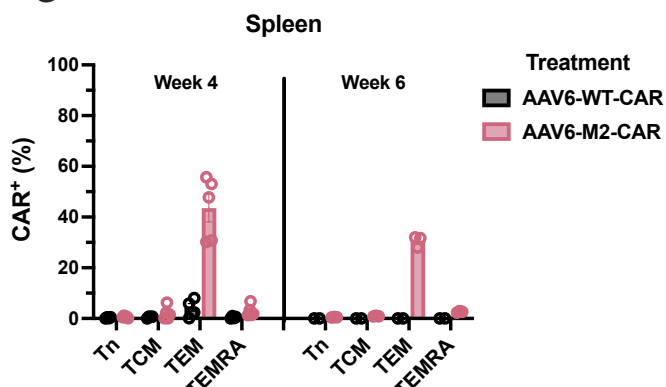
E



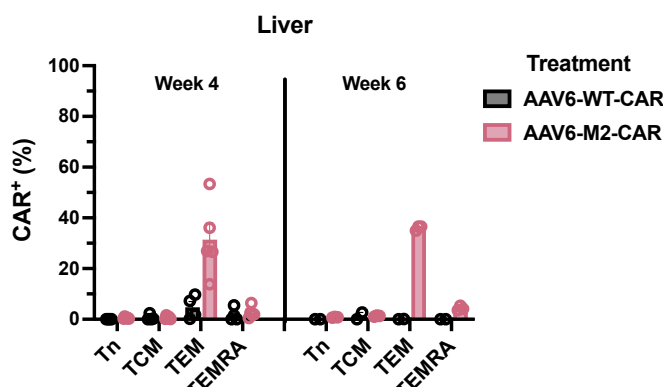
F



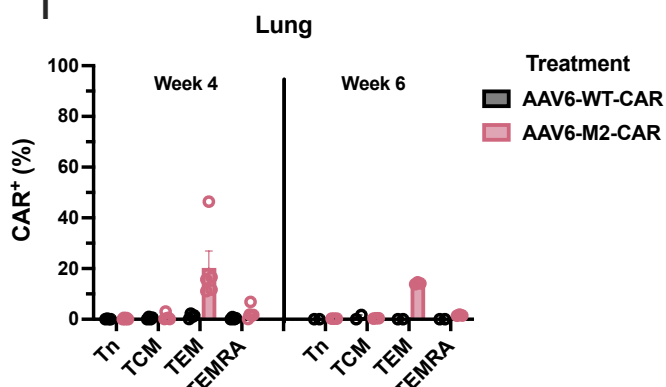
G



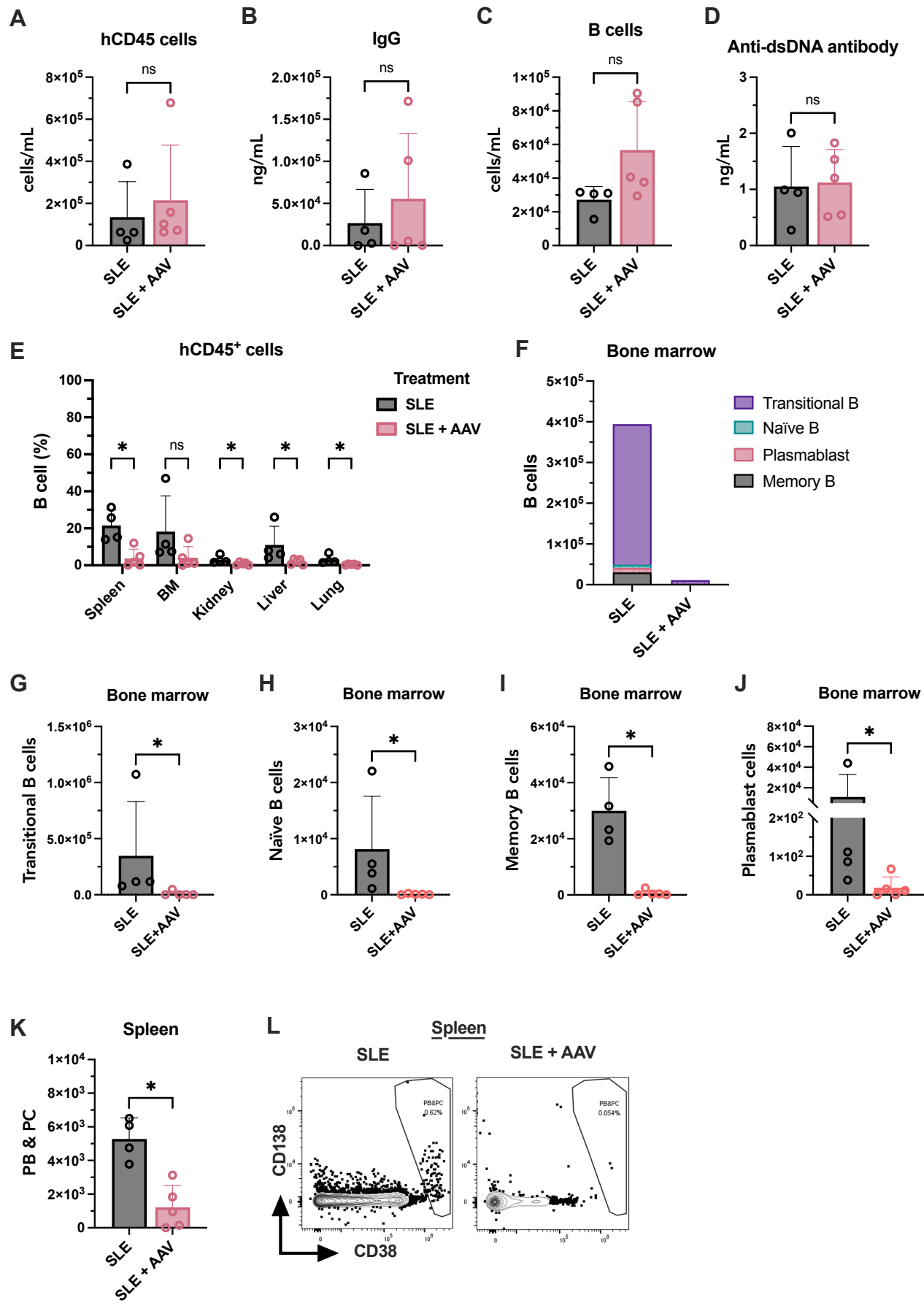
H



I



Supplementary Figure 5



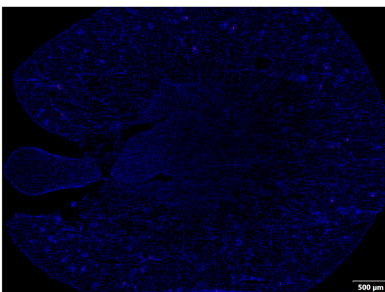
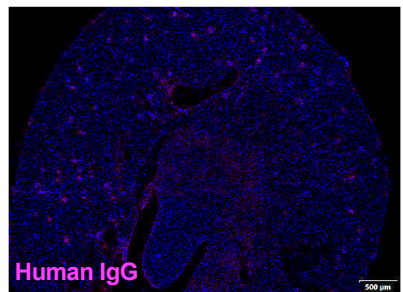
Supplementary Figure 5 (continued)

M

Kidney

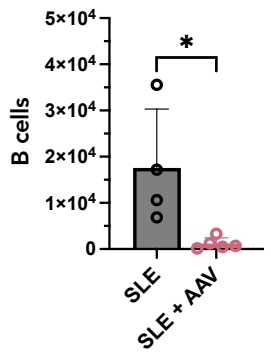
SLE

SLE + AAV



N

Lung

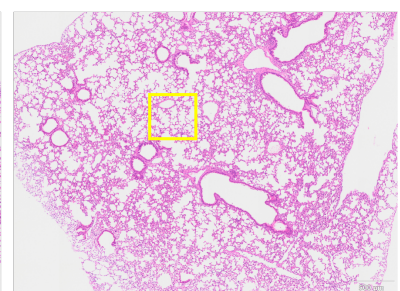
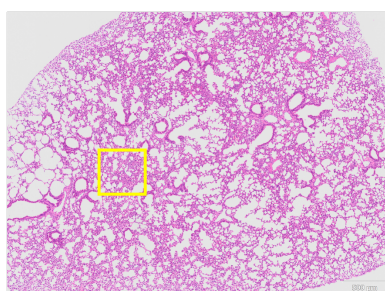


O

Lung

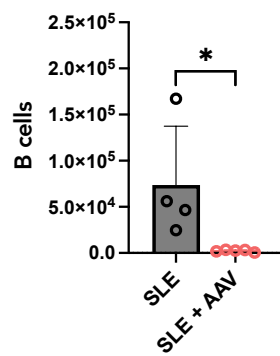
SLE

SLE + AAV



P

Liver

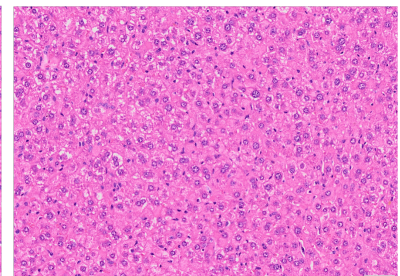
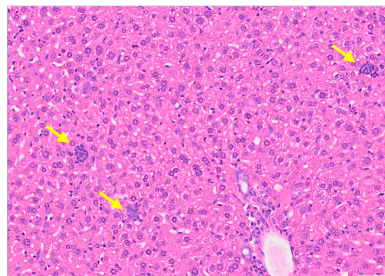


Q

Liver

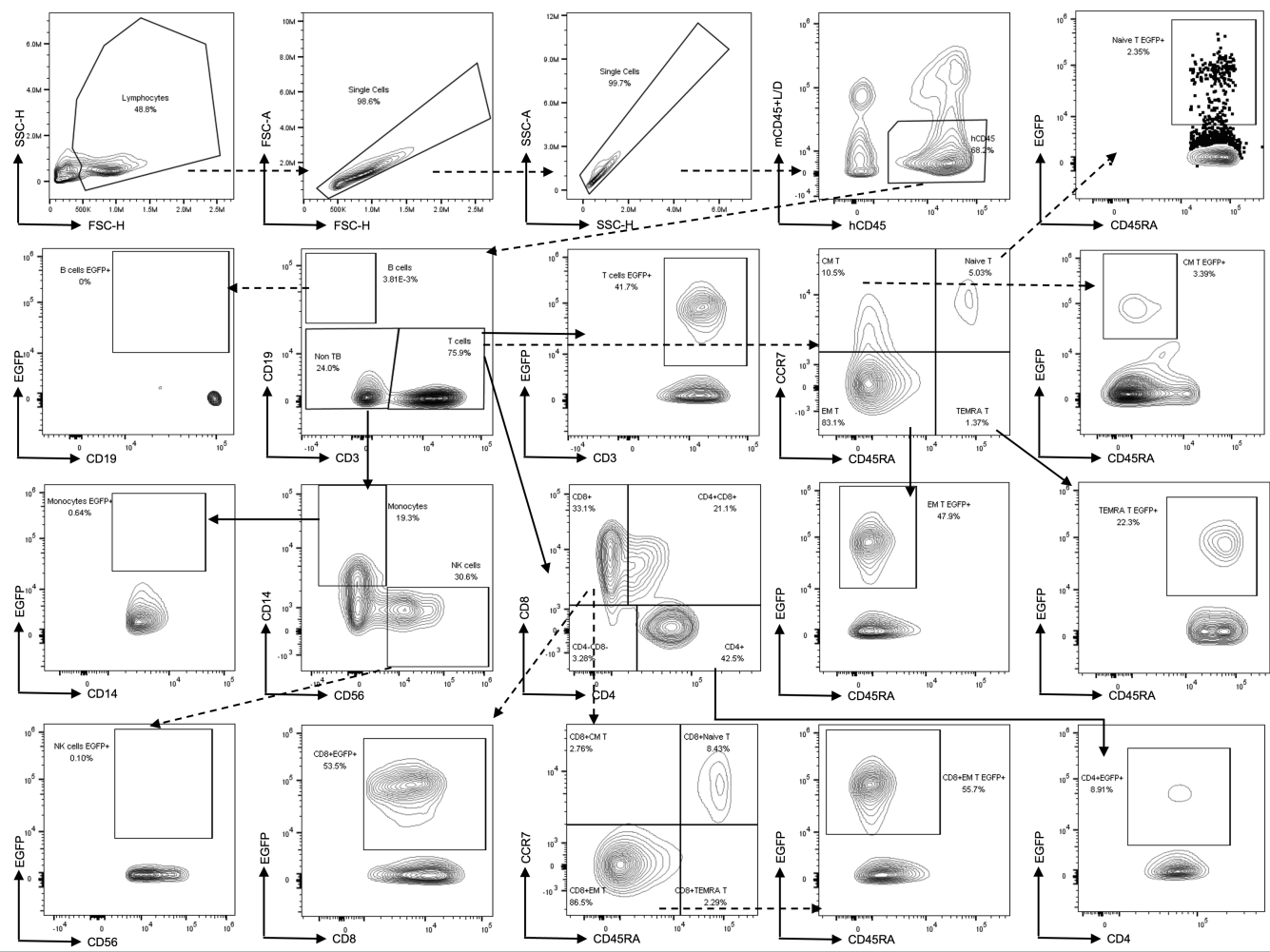
SLE

SLE + AAV



Supplementary Figure 6

A



B

